### **OPEN ACCESS**



# Hubble Space Telescope Proper Motion Measurements of Supernova Remnant N132D: Center of Expansion and Age

John Banovetz<sup>1,2</sup>, Dan Milisavljevic<sup>1,3</sup>, Niharika Sravan<sup>4</sup>, Kathryn E. Weil<sup>1</sup>, Bhagya Subrayan<sup>1</sup>, Robert A. Fesen<sup>5</sup>, Daniel J. Patnaude<sup>6</sup>, Paul P. Plucinsky<sup>6</sup>, Charles J. Law<sup>6</sup>, William P. Blair<sup>7</sup>, and Jon A. Morse<sup>8,9</sup>, braniel J. Patnaude<sup>6</sup>, Paul P. Plucinsky<sup>6</sup>, Charles J. Law<sup>6</sup>, William P. Blair<sup>7</sup>, and Jon A. Morse<sup>8,9</sup>, braniel J. Patnaude<sup>8</sup>, Paul P. Plucinsky<sup>6</sup>, Charles J. Law<sup>6</sup>, William P. Blair<sup>7</sup>, and Jon A. Morse<sup>8,9</sup>, braniel J. Patnaude<sup>9</sup>, Paul P. Plucinsky<sup>6</sup>, Charles J. Law<sup>6</sup>, William P. Blair<sup>7</sup>, and Jon A. Morse<sup>8,9</sup>, braniel J. Patnaude<sup>9</sup>, Paul P. Plucinsky<sup>6</sup>, Charles J. Law<sup>6</sup>, NY, USA, NY, USA

3 Integrative Data Science Initiative, Purdue University, West Lafayette, IN, 47907, USA

4 California Institute of Technology, 1200 E. California Boulevard, Pasadena, CA, 91125, USA

5 Department of Physics and Astronomy, 6127 Wilder Laboratory, Dartmouth College, Hanover, NH, 03755, USA

6 Center for Astrophysics | Harvard & Smithsonian, 60 Garden Street, Cambridge, MA, 02138, USA

7 The William H. Miller III Department of Physics and Astronomy, Johns Hopkins University, 3400 N. Charles Street, Baltimore, MD, 21218, USA

8 6 Boldly Go Institute, 31 W 34 St, Floor 7 Suite 7159, New York, NY, 10001, USA

9 Visiting Associate in Astronomy, Division of Physics, Mathematics and Astronomy, California Institute of Technology, Pasadena, CA, 91125, USA

Received 2022 August 23; revised 2022 December 4; accepted 2022 December 16; published 2023 May 3

#### Abstract

We present proper motion measurements of the oxygen-rich ejecta of the LMC supernova remnant N132D using two epochs of Hubble Space Telescope Advanced Camera for Surveys data spanning 16 years. The proper motions of 120 individual knots of oxygen-rich gas were measured and used to calculate a center of expansion (CoE) of  $\alpha=5^{\rm h}25^{\rm m}01^{\rm s}.71$  and  $\delta=-69^{\rm o}38'41''.64$  (J2000) with a  $1\sigma$  uncertainty of 2''.90. This new CoE measurement is 9''.2 and 10''.8 from two previous CoE estimates based on the geometry of the optically emitting ejecta. We also derive an explosion age of  $2770 \pm 500$  yr, which is consistent with recent age estimates of  $\approx 2500$  yr made from 3D ejecta reconstructions. We verified our estimates of the CoE and age using a new automated procedure that detected and tracked the proper motions of 137 knots, with 73 knots that overlap with the visually identified knots. We find that the proper motions of the ejecta are still ballistic, despite the remnant's age, and are consistent with the notion that the ejecta are expanding into an interstellar medium cavity. Evidence for explosion asymmetry from the parent supernova is also observed. Using the visually measured proper motion measurements and corresponding CoE and age, we compare N132D to other supernova remnants with proper motion ejecta studies.

Unified Astronomy Thesaurus concepts: Supernova remnants (1667); Interstellar medium (847) Supporting material: machine-readable table

### 1. Introduction

Supernova remnants (SNRs) provide valuable insights into the explosion processes of supernovae that are otherwise too distant to resolve (see Milisavljevic & Fesen 2017 for a review). They offer unique opportunities to probe the elemental distribution of metal-rich ejecta and investigate the progenitor star's mass-loss history at fine scales (see Lopez & Fesen 2018 for a review). Young, nearby oxygen-rich (O-rich) SNRs, created from the collapse of massive stars (zero-age main sequence, ZAMS, mass  $> 8 M_{\odot}$ ; Smartt 2009), are especially informative to study core-collapse dynamics because they are often associated with progenitor stars that were largely stripped of their hydrogen envelopes (e.g., Blair et al. 2000; Chevalier 2005; Temim et al. 2022). The kinematic and chemical properties of their metal-rich ejecta retain information about the parent supernova explosion that would otherwise be lost in an H-rich explosion (Milisavljevic et al. 2010).

Tracking metal-rich ejecta over many years and measuring their proper motions enable estimates of the center of expansion (CoE) and explosion age, as well as information about the progenitor system's circumstellar material (CSM) environment via ejecta interaction. The CoE and explosion age

Original content from this work may be used under the terms of the Creative Commons Attribution 4.0 licence. Any further distribution of this work must maintain attribution to the author(s) and the title of the work, journal citation and DOI.

are important values for determining the kick velocity of compact objects (Vogt et al. 2018; Banovetz et al. 2021; Long et al. 2022), searching for surviving companions (Kerzendorf et al. 2019; Li et al. 2021), and measuring differences between optical and X-ray centers (Katsuda et al. 2018). These values can also serve as important tests for increasingly sophisticated 2D and 3D supernova simulations (e.g., Wongwathanarat et al. 2015; Janka et al. 2016; Burrows et al. 2019; Ferrand et al. 2021; Orlando et al. 2021, 2022).

Only a handful of known O-rich SNRs are sufficiently resolved to measure the proper motions of high-velocity ejecta from multi-epoch observations. This small list includes Cassiopeia A (Cas A; Kamper & van den Bergh 1976; Thorstensen et al. 2001; Fesen et al. 2006; Hammell & Fesen 2008), G292.0+1.8 (G292; Murdin & Clark 1979; Winkler et al. 2009), and 1E 0102.2–7219 (E0102; Finkelstein et al. 2006; Banovetz et al. 2021). This paper focuses on the O-rich SNR N132D, which to date has no published proper motion measurements of its optically emitting ejecta.

N132D is located in the bar of the Large Magellanic Cloud (LMC) and was first identified as an SNR from radio emission (Westerlund & Mathewson 1966). Later, it was found to contain high-velocity O-rich ejecta through optical spectra, classifying it as an O-rich SNR (Danziger & Dennefeld 1976; Lasker 1980). The parent supernova may have been a Type Ib with a 10–35  $M_{\odot}$  ZAMS progenitor (Blair et al. 2000; Sharda et al. 2020). Presently, the SNR continues to expand into a

Table 1 HST Observations of N132D

PI	Date	Exp. Time (s)	Instrument	Filter	$\lambda_{ ext{center}} \ ( ext{Å})$	Bandwidth (Å)	Pixel Scale (" pixel <sup>-1</sup> )
Blair	1994-08-09	3600	WFPC2/PC	F502N	5012	27	0.0455
Green	2004-01-22	1440	ACS/WFC	F658N	6584	75	0.049
Green	2004-01-22	1800	ACS/WFC	F550M	5580	389	0.049
Green	2004-01-21	1440	ACS/WFC	F775W	7702	1300	0.049
Green <sup>a</sup>	2004-01-22	1520	ACS/WFC	F475W	4760	1458	0.049
Milisavljevic <sup>a</sup>	2020-01-05	2320	ACS/WFC	F475W	4760	1458	0.049
Milisavljevic	2020-01-05	2480	WFC3/UVIS	F502N	5013	48	0.040

#### Note.

cavity created by the pre-supernova mass loss of the progenitor star (Hughes 1987; Sutherland & Dopita 1995; Blair et al. 2000; Chen et al. 2003; Sharda et al. 2020).

N132D is the brightest X-ray and gamma-ray SNR in the LMC (Clark 1982; Favata et al. 1997; Borkowski et al. 2007; H.E.S.S. Collaboration et al. 2015; Ackermann et al. 2016). X-ray images show a horseshoe-shaped forward shock (e.g., Borkowski et al. 2007; Bamba et al. 2018), the southern portion of which is associated with natal molecular clouds (Banas et al. 1997; Dopita et al. 2018; Sano et al. 2020). X-ray and radio observations indicate that N132D is transitioning from a young to middle-aged SNR and is about to enter the Sedov phase (Dickel & Milne 1995; Favata et al. 1997; Bamba et al. 2018).

Previous estimates of N132D's explosion age have been made by dividing the radius of the SNR by the maximum radial velocity of the ejecta, yielding age estimates ranging from 1300 to 3440 yr (Danziger & Dennefeld 1976; Lasker 1980; Morse et al. 1995; Sutherland & Dopita 1995). Morse et al. (1995) gave two estimates for the CoE of N132D. The first estimate was made by fitting an ellipse to the diffuse outer rim, and the second by finding the geometric center of the O-rich ejecta. Recent 3D reconstructions of N132D use this geometrically derived center as the CoE and find that N132D's optically emitting O-rich material is arranged in a torus distribution, inclined at an angle of  $\approx 25^{\circ}-28^{\circ}$  in the plane of the sky (Vogt & Dopita 2011; Law et al. 2020). They also provide the most recent age estimates of  $\approx 2500$  yr.

This paper uses high-resolution images obtained with the Hubble Space Telescope (HST) to measure the proper motions of N132D's O-rich ejecta to estimate the CoE and explosion age. Section 2 discusses observations of N132D and the images used. Section 3 describes our proper motion measurements and analysis techniques. Section 4 introduces an automated procedure to measure proper motions using computer vision (more details in the Appendix). Section 5 discusses the implications of the proper motion measurements, CoE, and explosion age as they pertain to previous estimates and other SNRs. We summarize and conclude in Section 6.

### 2. Observations

Using the Mikulski Archive for Space Telescopes (MAST) at the Space Telescope Science Institute, we examined three epochs of HST images that are sensitive to  $[O III] \lambda\lambda 4959$ , 5007 emission tracing the O-rich ejecta of N132D.<sup>10</sup> These

consist of an image taken in 1994 using the Wide Field Planetary Camera 2 (WFPC2) with the F502N filter (PI: Blair GO-5365), a 2004 image using the the Advanced Camera for Surveys (ACS) and the F475W filter (PI: Green GO-12001), and a 2020 image using the ACS/F475W setup (PI: Milisavljevic GO-15818). The 1994 and 2020 F502N images use different instrument and filter configurations, whereas the 2004 and 2020 F475W images were both obtained with ACS. Utilizing the same camera/filter setup greatly improves the tracking confidence of the gas, as using different camera/filters setups can cause ambiguity in precise tracking due to brightening effects (see Banovetz et al. 2021). Thus, only the ACS images were used for proper motion tracking. The 2020 F502N image was used to confirm the O-rich ejecta emission from any possible continuum emission. All images were processed using Astrodrizzle (Gonzaga et al. 2012) and had a final image scale of approximately 0.05 pixel<sup>-1</sup>. Table 1 contains more information about the images used for the analysis.

To align the images, we use the geomap task in PYRAF<sup>11</sup> to create a transformation database using 30 anchor stars between the two images (see Table A1 in the Appendix). These anchors were chosen for their low proper motions and small transformation residuals. The transformation had resulting residuals of  $\approx 0.3$  pixels ( $\approx 0.0015$ ). We then used the PYRAF task geotran to apply this transformation, aligning the images. Once the images were aligned, they were cropped to a  $51.75 \times 58.73$  field of view that contains only the O-rich portion of the remnant (see Figure 1). The cropping extent was determined by visual examination of the oxygen emission, and we ensured that all high proper motion ejecta knots were contained within the selected field of view. The world coordinate system (WCS) was calculated using a locally compiled version of Astrometry. net <sup>12</sup> (Lang et al. 2010). This WCS solution is accurate to  $\approx 0.^{\prime\prime}$ 17 and was taken into account for the final CoE error.

## 3. Proper Motion Measurements: Manual Estimation

Using the aligned images, we identified knots with high proper motions. Knots were chosen by how well they could be tracked visually, with most knots being optically bright and

<sup>&</sup>lt;sup>a</sup> Denotes images used in the proper motion analysis.

<sup>&</sup>lt;sup>10</sup> The specific observations analyzed can be accessed via DOI:10.17909/ 4ppy-4e90.

PYRAF is distributed by the National Optical Astronomy Observatory, which is operated by the AURA, Inc., under cooperative agreement with the National Science Foundation. The Space Telescope Science Data Analysis System (STSDAS) is distributed by STScI.

Astrometry.net is distributed as open source under the GNU general

public license and was developed on Linux.

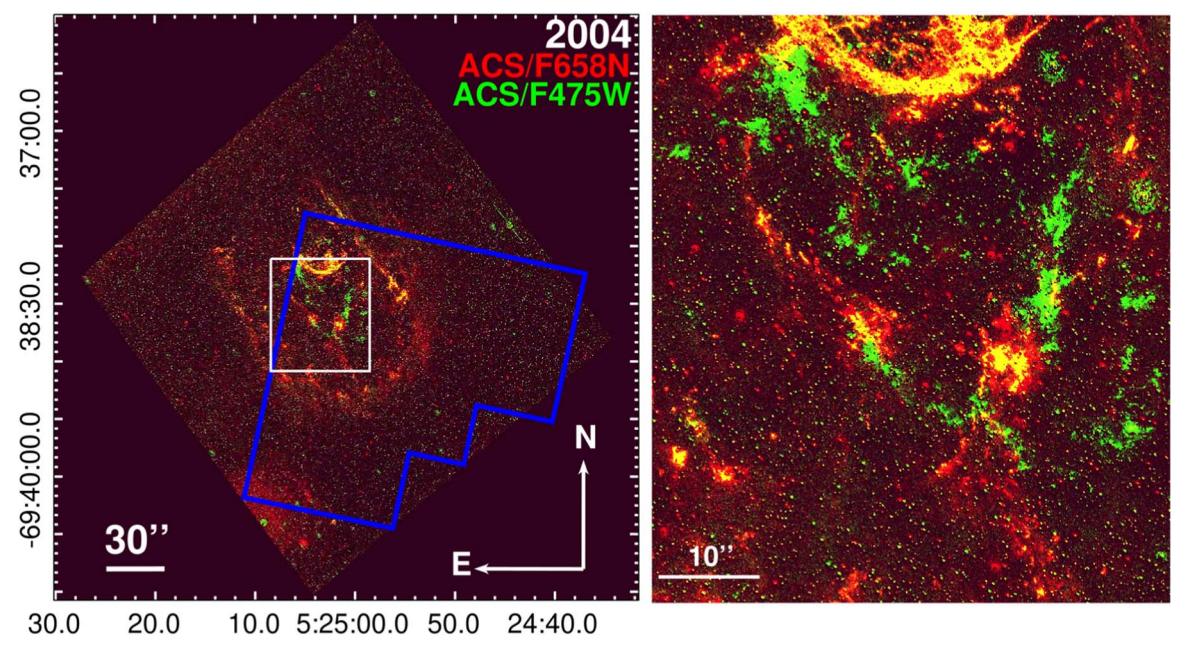


**Figure 1.** Left: continuum-subtracted image of N132D using images taken with HST/ACS and the F475W (green) and F658N (red) filters (additional image information can be found in Table 1). The blue polygon indicates the field of view of the 1994 WFPC2/F502N image. The white square is the cropped image of N132D used for the proper motion measurements. Right: enlarged view of the white square, highlighting in green the O-rich ejecta used for the proper motion measurements.

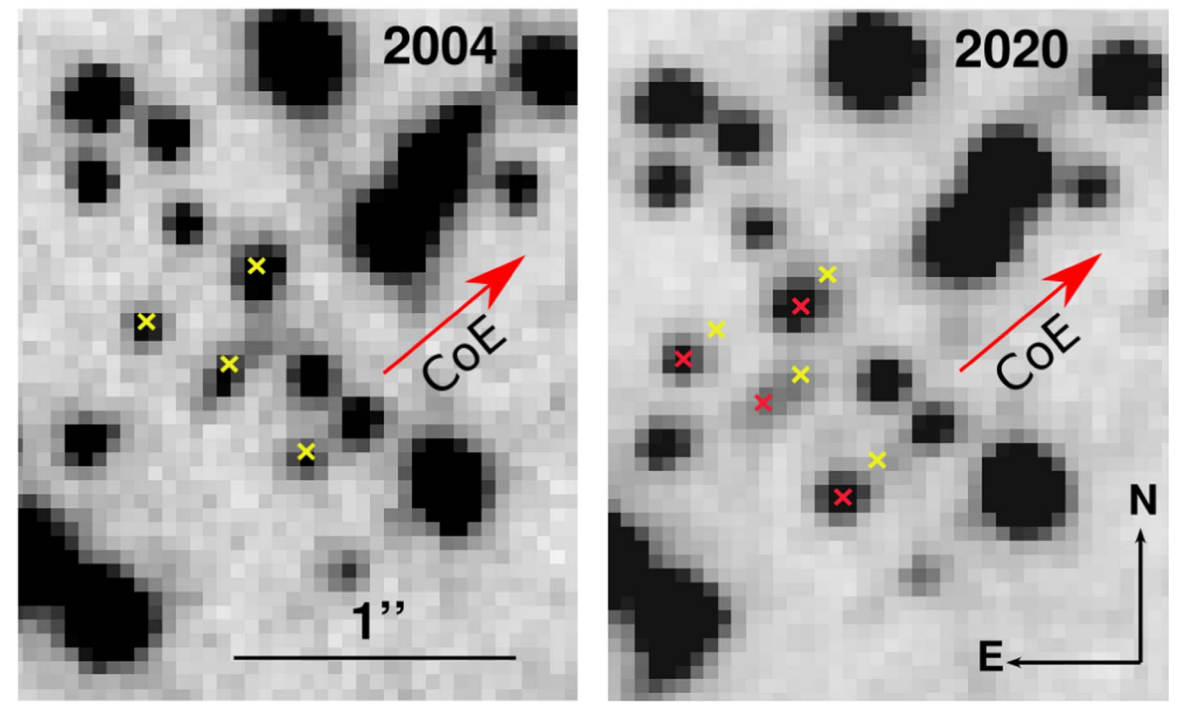


**Figure 2.** ACS/F475W images showing examples of the expanding ejecta knots in 2004 (left) and 2020 (right) in the area of the RK (see Section 5.1 for more details). The 2004 knot centroids are shown as yellow crosses while the 2020 centroids are shown as red crosses. The red arrow points in the direction of the CoE.

circular to have confidence in the measurements. The shifts of the knots were calculated by blinking between the two images in SAOImage DS9 and visually locating the centers of the knots or other conspicuous features (see Figure 2). The centers were measured multiple times to estimate the positional errors of each knot. During the 16 years, knots can possibly brighten/dim or change morphology as they interact with the surrounding medium (Fesen et al. 2011; Banovetz et al. 2021). This interaction can skew results if using the astrometric

approach of fitting a Gaussian to the knots. We did apply a Gaussian-based centroid fitting procedure (see the Appendix and Section 4) and found more accurate results through manual inspection.

We applied our methodology to 120 knots (see Table A2 in the Appendix), which resulted in proper motions ranging from 3 to 14.5 milliarcseconds (mas) per year, with a median proper motion of 7.54 mas yr<sup>-1</sup> and an average relative error of 13% (Figure 3). This translates to a median velocity of 1784

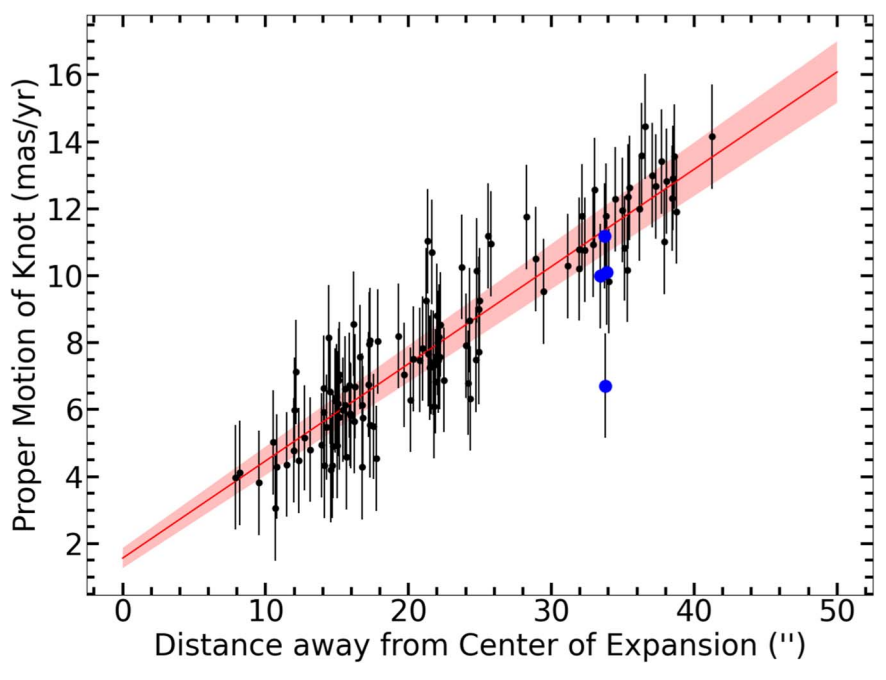


Figure 3. The absolute proper motions vs. radial distances of the knots. The proper motions of the knots of ejecta are shown as black points with their corresponding  $1\sigma$  errors. The red line indicates a linear fit to the data with the shaded region indicating the  $1\sigma$  error. The locations of the four knots in the RK region are highlighted as blue points.

km s<sup>-1</sup> assuming a distance to the LMC of 50 kpc (Panagia et al. 1991). Our median velocity is consistent within the uncertainties to the average expansion velocity of 1745 km s<sup>-1</sup> calculated using a fitted projected radius of N132D (Law et al. 2020). The linear fit also gives a higher scaling factor *S* of 0."014 per km s<sup>-1</sup> compared to 0."010 per km s<sup>-1</sup> of Law et al. (2020). Figure 4 shows the locations and proper motions of the 120 knots, as well as the O-rich regions discussed in Morse et al. (1995).

## 3.1. CoE Calculation

Our approach to determine the CoE of N132D uses the trajectories of the ejecta augmented with a likelihood function. This method is similar to those used by Banovetz et al. (2021) and Thorstensen et al. (2001) for the calculation of E0102's and Cas A's CoE, respectively. We favor this method because it only depends on the direction of the knots, and is not sensitive to deceleration over time.

We assume that the likelihood of the CoE in the plane of sky coordinates (x, y) is given by:

$$\mathcal{L}(X, Y) = \prod_{i} \frac{w_i}{2\sigma_i} \exp(-d_{i\perp}^2/(2\sigma_i^2)), \tag{1}$$

$$w_i = \frac{1}{P_{y_i} P_{x_i}},\tag{2}$$

where  $d_{i\perp}$  is the perpendicular distance between (x, y) and the knot's line of position and  $\sigma_i$  is the uncertainty associated with the point common to the knot's extended line of position and  $d_{i\perp}$  (Banovetz et al. 2021). We also define w, the probability of finding an individual knot in a given x and y position, denoted by  $P_{x_i}$  and  $P_{y_i}$ , respectively, which was calculated using a kernel density estimate (KDE) to fit knots in the (x, y) plane. The (x, y) combination that maximizes this function gives the CoE. The uncertainty of the CoE is derived from 100,000 artificial data

sets generated from the position and direction distributions of the individual knots.

A notable difference from Banovetz et al. (2021) is the addition of a weight, w. We used this weight to minimize the effects of selection bias in our sample. As seen in Figure 4, N132D is unique compared to other O-rich SNRs in that the knot distribution is skewed, with a larger number of knots displaying proper motions in the northern region of the remnant as compared to the southern region. Without the weight, the CoE will skew in the direction of the more populated region. This added weight term compensates for sparse regions by giving proportionally more weight to knots in these regions.

Applying this procedure to our proper motion measurements yields a CoE of  $\alpha = 5^{\rm h}25^{\rm m}01^{\rm s}.71$  and  $\delta = -69^{\circ}38'41''.64$  (J2000) with a  $1\sigma$  uncertainty of 2''.90. Figure 5 shows the trajectories of the knots as compared to the derived CoE.

### 3.2. Explosion Age

Using the manually tracked knots and the associated CoE estimate, we calculated the explosion age of N132D by dividing the knot's distances from the CoE by their proper motion measurements. Figure 6 shows the calculated explosion age of all 120 knots. Combining these ages resulted in an age of  $2770 \pm 500$  yr.

We also calculated the explosion age using only the knots with the fastest proper motions. A similar approach was used by Fesen et al. (2006) for the explosion age of Cassiopeia A and Banovetz et al. (2021) for E0102. This method assumes that knots with the fastest proper motions are least decelerated, resulting in a more accurate explosion age. 49 of the 120 knots with proper motions greater than the average (8.1 mas yr<sup>-1</sup>) were selected. Almost all these knots correspond to region B4 from Morse et al. (1995). Using these knots resulted in an explosion age of  $2745 \pm 404$  yr, consistent with the age using

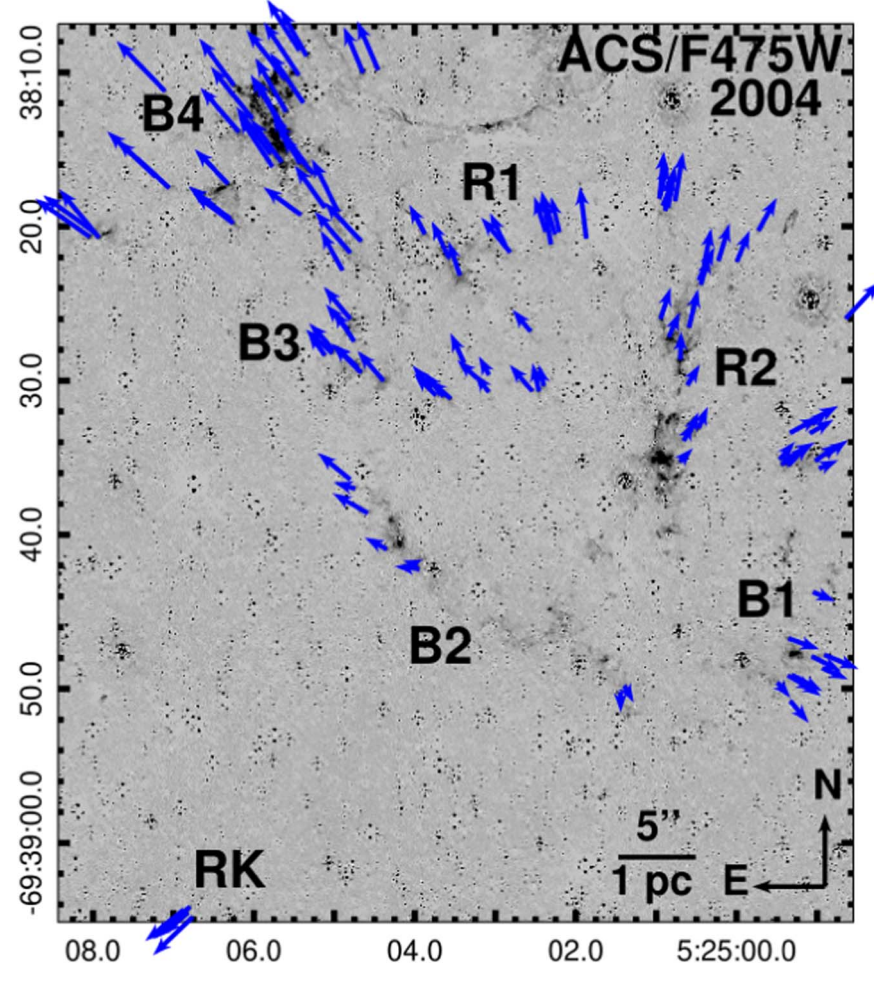


Figure 4. 2004 ACS/F475W continuum- and hydrogen-subtracted image with vectors representing the measured shifts (multiplied by a factor of 20 for visual clarity) shown in blue. The regions identified in Morse et al. (1995) are also labeled.

all of the knots. For further discussion, we adopt the age of  $2770 \pm 500$  yr, as this age is representative of all the knots.

# 4. Proper Motion Measurements: Automated via Computer Vision

We also implemented a novel computer vision based approach to measure the proper motions of the ejecta. This approach utilizes hydrogen- and continuum-subtracted images between the epochs to insure that only the O-rich material is being tracked. Then, regions of high emission and/or high ejecta proper motions are specified. These regions, or stamps, are passed through an automated detection procedure to identify knots using image segmentation and deblending. To track the knots, a KDE estimates the peaks within these segments, and we use these peaks to measure the proper motion between the epochs. A more detailed explanation of this procedure can be found in the Appendix.

The automated procedure identified and measured the proper motions of 137 knots of ejecta. The average difference in the inferred values between the manual and automated procedures for the shift between epochs is  $0.0^{\circ}$ 03 (or  $\approx 1.8$  mas yr<sup>-1</sup>) and the vector angle is  $\approx 12^{\circ}$ . The

error of the proper motions was set to 0.4 pixels ( $\approx$ 0."2), from the sub-pixel ratio of the KDE. While the automated proper motion measurements generally followed the same ballistic  $v \propto r$  relationship found with the visually tracked knots, the measurements exhibited more scatter and higher uncertainties. This discrepancy most likely arises from tracking fainter, less-dense knots that are more susceptible to deceleration compared to the bright, denser knots that were found visually.

While our automated procedure generally produces similar results to the visually measured proper motions, the sample is contaminated by the less-dense knots, possibly skewing the results. Hence, we adopt the visual measurement results for this paper. We note that the results above used conservative metrics in the measurement of the proper motions in order not to be biased too heavily by any one parameter. Attempts to improve the results by fine-tuning these parameters can be found in the Appendix.

## 5. Discussion

## 5.1. Proper Motion Measurements

Our work presents the first proper motion measurements of the O-rich ejecta of N132D. We visually identified and tracked 120 knots of ejecta across 16 years. While the baseline is large and could be on the order of shock cooling times, we are confident in our tracking ability. This is because the emission

 $<sup>\</sup>overline{^{13}}$  The proper motion measurements and locations can be found in a machine-readable format, a subset of which can be found in Table A2.

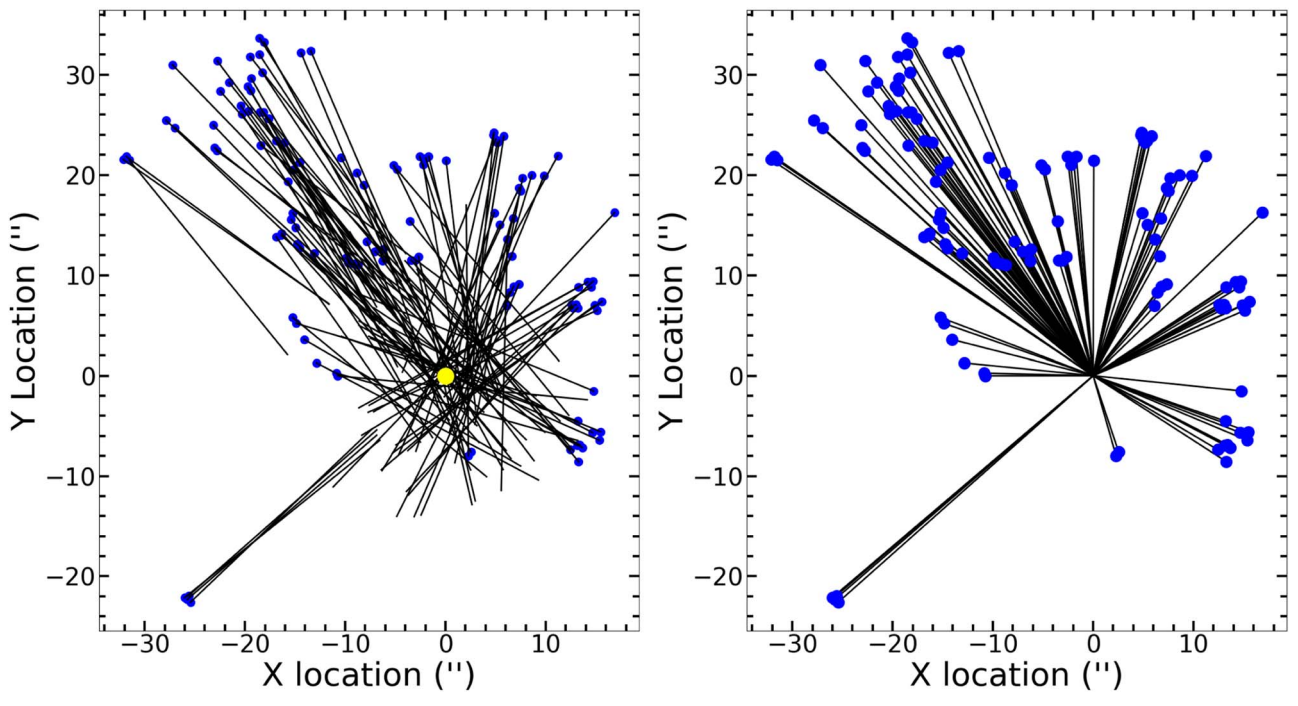
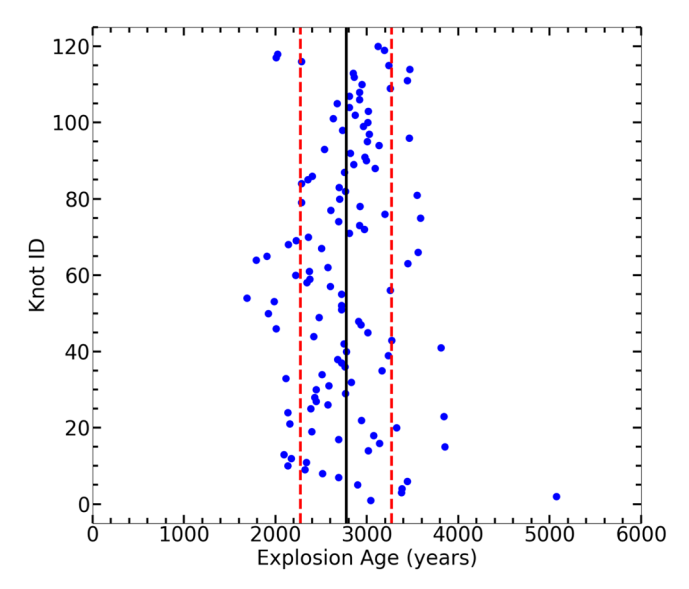


Figure 5. Left: the visually measured proper motions of the 120 knots traced back 25'' ( $\approx 3000$  yr assuming an average proper motion of 8.1 mas yr<sup>-1</sup>). The CoE is shown in yellow. Right: the trajectories of the visually measured knots if forced to originate from our calculated CoE. Strong spatial asymmetry in the knot distribution is observed with respect to the CoE.



**Figure 6.** A comparison of the explosion age measurements, assuming our CoE. The black line represents the average age of the data set, while the red dashed lines show the  $1\sigma$  uncertainty. This results in an explosion age of  $2770 \pm 500$  yr.

mechanism is most likely a combination of shock excitation and photoionization producing a high amount of [O III] emission (Sutherland & Dopita 1995), the low densities of the shock will increase the cooling times (Blair et al. 2000), and we find similar morphology in the knots between epochs. With these 120 knots, we find that the ejecta follow homologous expansion with an average proper motion of 8.1 mas yr<sup>-1</sup> (median proper motion of 7.54 mas yr<sup>-1</sup>) despite N132D's advanced age approaching the Sedov phase.

Figure 3 shows the proper motions of the knots versus their distances away from our calculated CoE (see Section 3.1).

Comparing this with spectroscopic measurements, the highest proper motion measurements are seen in the B4 region, as first reported in Morse et al. (1995), and shown in the left panel of Figure 4. This is to be expected, as B4 corresponds to a region of small Doppler velocities in the O-rich ejecta (Morse et al. 1995; Vogt & Dopita 2011; Law et al. 2020), as seen in the upper left of the plot in the right panel of Figure 7. We find this inverse relationship between the proper motion measurements and Doppler velocities to hold true except for region B1. B1 also corresponds to an area of small Doppler velocities, but the proper motion measurements are much smaller compared to those in B4. This difference in proper motions could be a result of B1 possibly being outside the reverse shock, as proposed by Vogt & Dopita (2011; see Figure 7 for X-ray emission tracing the shocks). However, as this region is consistent with the ballistic trend, it is more likely associated with an explosion asymmetry (see Section 5.3 for more discussion).

Notably, the fit shown in Figure 3 does not pass through the origin and has an offset of  $\approx+1.6$  mas yr $^{-1}$ . Forcing the line through the origin results in  $S\approx0.0^{\circ}0.12$  per km s $^{-1}$ , which is closer to the value reported in Law et al. (2020). This offset in the original fit could be indicative of deceleration experienced by the ejecta over time. As the ejecta expands in the surrounding environment, the fastest ejecta will interact and decelerate at a different rate compared to the slower ejecta. This will disrupt the  $v \propto r$  relation between the ejecta velocity and distance from the CoE, introducing a positive offset term to the linear fit.

A unique feature of N132D is the runaway knot (RK), which is an isolated small clump of ejecta located in the southwestern portion of the remnant and is unique in that it is enhanced in Si and S but not O (Law et al. 2020). The RK was first reported in Morse et al. (1995) and recent 3D reconstructions show that the knot is perpendicular to the main torus (Vogt & Dopita 2011; Law et al. 2020). Explanations for the origin of the RK include

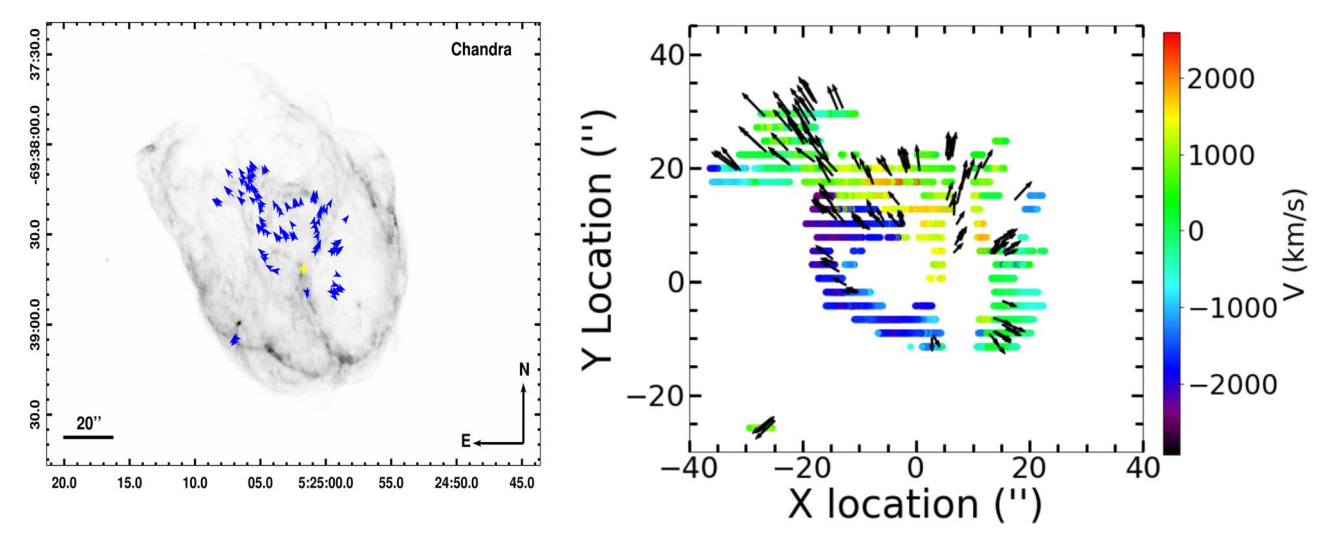


Figure 7. Left: Chandra image of N132D (PI: Borkowski). The proper motions from the visual measurements are in blue and our calculated CoE is in yellow (see Section 3.1). Right: vectors of the proper motions (black) with Doppler velocities (Law et al. 2020), centered on our CoE (see Section 3.1).

evidence of a polar jet (Vogt & Dopita 2011) and high-velocity ejecta, similar to Cas A (Fesen & Gunderson 1996; Law et al. 2020). We were able to find and measure the proper motions of four O-rich knots in the same region as the RK (see Figures 2 and A2). The proper motions are faster than the global average but are still consistent with the proper motions of the other knots ( $\approx$ 9.5 mas yr<sup>-1</sup> or  $\approx$ 2250 km s<sup>-1</sup>). Combining this with a Doppler velocity of 820 km s<sup>-1</sup> (Law et al. 2020), the RK has a 3D velocity of  $\approx$ 2395 km s<sup>-1</sup>. This is much slower than the total spatial velocity of  $\approx$ 3650 km s<sup>-1</sup> calculated by Law et al. (2020), which is a consequence of using a scaling relation found from the innermost ejecta that was then extended to the RK.

Although we conclude that the RK does not have kinematic features that distinguish it from the bulk of N132D's ejecta, there remains a conspicuous gap in the proper motion measurements in the direction of the RK and our analysis was unable to uncover any new rapidly moving ejecta in this location. The isolated nature of the RK may imply that it passed through the reverse shock and only recently became optically bright again due to interaction with the CSM/interstellar medium (ISM). This interpretation is supported by X-ray enhancement in close proximity to the RK (Borkowski et al. 2007; Law et al. 2020), which can be seen in the left panel of Figure 7, where the RK is located in the southeast, very close to the rim of X-ray emission. Further observations of this area may reveal more knots interacting with the CSM/ISM and fill the conspicuous gap.

# 5.2. CoE and Age Results

In Figure 10, we compare our resulting visually inspected CoE to the estimates from Morse et al. (1995) and the automated procedure (see Section 4 for more details) in Figure 8. Our estimate is located 9."2 to the southwest of the oxygen geometric center and 10."8 to the south and slightly east from the geometric center of the diffuse rim. Notably, these geometric center estimates are  $\approx 3.2\sigma$  and  $3.7\sigma$  away from our estimate, respectively. Our new age estimate of  $2770 \pm 500$  yr is consistent with the value of  $\approx 2500$  yr estimated by Vogt & Dopita (2011) and Law et al. (2020), as well as the estimate of  $2350 \pm 520$  yr made by Sutherland & Dopita (1995).

## 5.3. Comparison to Other O-rich SNRs

With our new proper motion measurements of the optically emitting ejecta of N132D, we expand the number of young (<3000 yr) O-rich SNRs with proper motion studies from three to four. <sup>14</sup> Table 2 shows the properties of these remnants (E0102, Cas A, and G292) compared to those of N132D. Figure 9 displays the positions of the O-rich knots with respect to their respective CoEs in physical space.

Compared to the three other SNRs, N132D shows the highest degree of spatial asymmetry in the distribution of high-velocity ejecta knots. The majority of the knots are seen to the north of the CoE. Given that the CSM/ISM in the northwest is associated with higher densities than in the south (Williams et al. 2006), this unique morphology is likely strongly influenced by explosion asymmetry. Further supporting the notion that N132D was an asymmetric explosion in a uniform environment is the ballistic proper motions we measure, the overall blueshift in the Doppler velocities of the ejecta (Lasker 1980; Morse et al. 1995; Sutherland & Dopita 1995; Vogt & Dopita 2011; Law et al. 2020), asymmetry in the elemental abundances in the X-ray observations (Sharda et al. 2020), and evidence of a bipolar explosion from 3D reconstructions (Vogt & Dopita 2011).

In contrast, the distribution of high-velocity ejecta knots in E0102 is fairly uniform, with only the northern part of the remnant lacking any high proper motion knots (Vogt et al. 2017). There is also a notable asymmetry in the proper motions, showing evidence that E0102 is now undergoing non-homologous expansion of optical ejecta (Banovetz et al. 2021). Proper motion measurements show non-ballisitic motion, with slower material occurring preferentially in the east (Banovetz et al. 2021), suggesting that E0102 is likely interacting with an inhomogenous surrounding environment. X-ray studies also show varying densities across the remnant, as well as a nonspherical forward shock (Sasaki et al. 2006; Xi et al. 2019). While some level of explosion asymmetry may be present, E0102's morphology is most likely dominated by effects from an inhomogenous surrounding environment.

<sup>14</sup> Work on Puppis A reported by Winkler et al. (2010) remains unpublished.

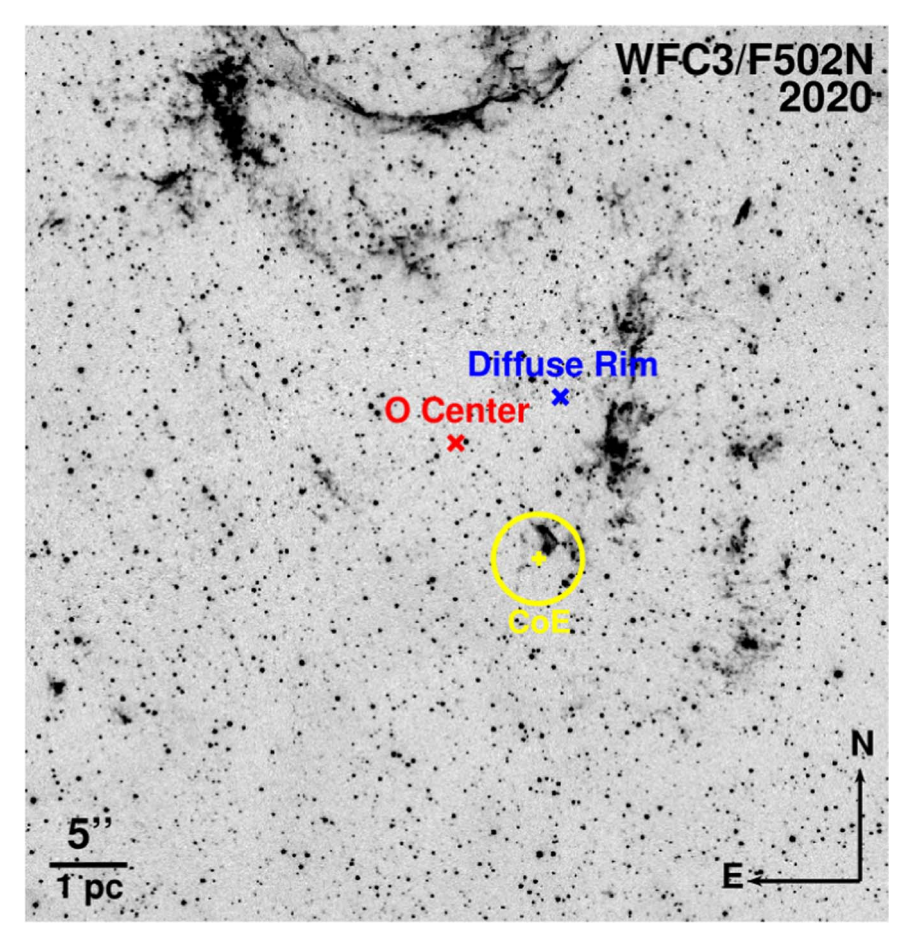


Figure 8. CoE estimates for N132D. This paper's CoE calculation and associated  $1\sigma$  uncertainty are shown in yellow. This CoE is centered at  $\alpha = 5^{\rm h}25^{\rm m}01^{\rm s}71$  and  $\delta = -69^{\circ}38'41\rlap.{''}64$  (J2000) with a  $1\sigma$  uncertainty of  $2\rlap.{''}90$ , and is  $9\rlap.{''}2$  and  $10\rlap.{''}8$  away from the estimates of Morse et al. (1995) found by fitting an ellipse to the diffuse outer rim (blue) and the O-rich geometric center (red).

Table 2
Characteristics of the Young O-rich SNRs

Parameter	G292	E0102	Cas A	N132D
Proper motion-derived CoE (J2000)	11:24:34.4 [1]	1:04:02.48 [2]	23:23:27.77 [3]	5:25:01.71 <sup>a</sup>
	-59:15:51	-72:01:53.92	+58:48:49.4	-69:38:41.64
CoE $1\sigma$ Error (")	5	1.77	0.4	2.90
Center of X-ray emission (J2000)	11:24:33.1 [4]	01:04:1.964 [5]	23:23:27.9 [4]	5:25:03.08 <sup>b</sup>
	-59:15:51.1	-72:01:53.47	58:48:56.2	-69:38:32.6
Current age (yr)	~2990 [1]	~1740 [2]	~350 [3]	$\sim 2770^{\rm a}$
Distance to remnant (kpc)	$6.2 \pm 0.9$ [7]	$62.1 \pm 1.9$ [8,9]	$3.4_{-0.1}^{+0.3}$ [10]	$50.1 \pm 3.1 \; [11]$
Size of remnant (arcmin)	8.4-9.6 [12]	0.7 [5]	5.6 [13]	1.8 [14]
Ejecta transverse velocity (km/s)	~1500-3600 [1]	~1300–2700 [2]	~5500–14500 [15]	$\sim 700-3400^{a}$
Progenitor ZAMS mass $(M_{\odot})$	13–30 [16]	25–50 [17,18]	15–20 [19]	10-35 [17,20]

References. [1] Winkler et al. (2009), [2] Banovetz et al. (2021), [3] Thorstensen et al. (2001), [4] Katsuda et al. (2018), [5] Xi et al. (2019), [6] Dickel & Milne (1995), [7] Gaensler & Wallace (2003), [8] Graczyk et al. (2014), [9] Scowcroft et al. (2016), [10] Reed et al. (1995), [11] Panagia et al. (1991), [12] Park et al. (2007), [13] Vink et al. (2022), [14] Law et al. (2020), [15] Fesen et al. (2006), [16] Bhalerao et al. (2019), [17] Blair et al. (2000), [18] Finkelstein et al. (2006), [19] Lee et al. (2014), and [20] Sharda et al. (2020).

G292, which is elongated along the north–south direction, shows very little evidence of an inhomogenous environment and its shape comes mostly from explosion asymmetry. Both proper motion studies and Doppler measurements show an asymmetric nature to the explosion (Ghavamian et al. 2005; Winkler et al. 2009). The proper motion-derived CoE coinciding with the X-ray and radio centers of emission (Winkler et al. 2009) also

support the notion of minimal CSM interaction. Despite interaction with an equatorial bar of CSM material, overall G292 appears to be expanding into a low-density environment (Ghavamian et al. 2005). However, CSM interactions cannot be ruled out. Recent simulations show that inhomogenous surrounding environments are reflected in the forward and reverse shock for only  $\approx\!2000~\rm yr$  (Orlando et al. 2022). There is

<sup>&</sup>lt;sup>a</sup> This work.

<sup>&</sup>lt;sup>b</sup> Estimated using archival Chandra observations (L. Xi et al. 2022, private communication).

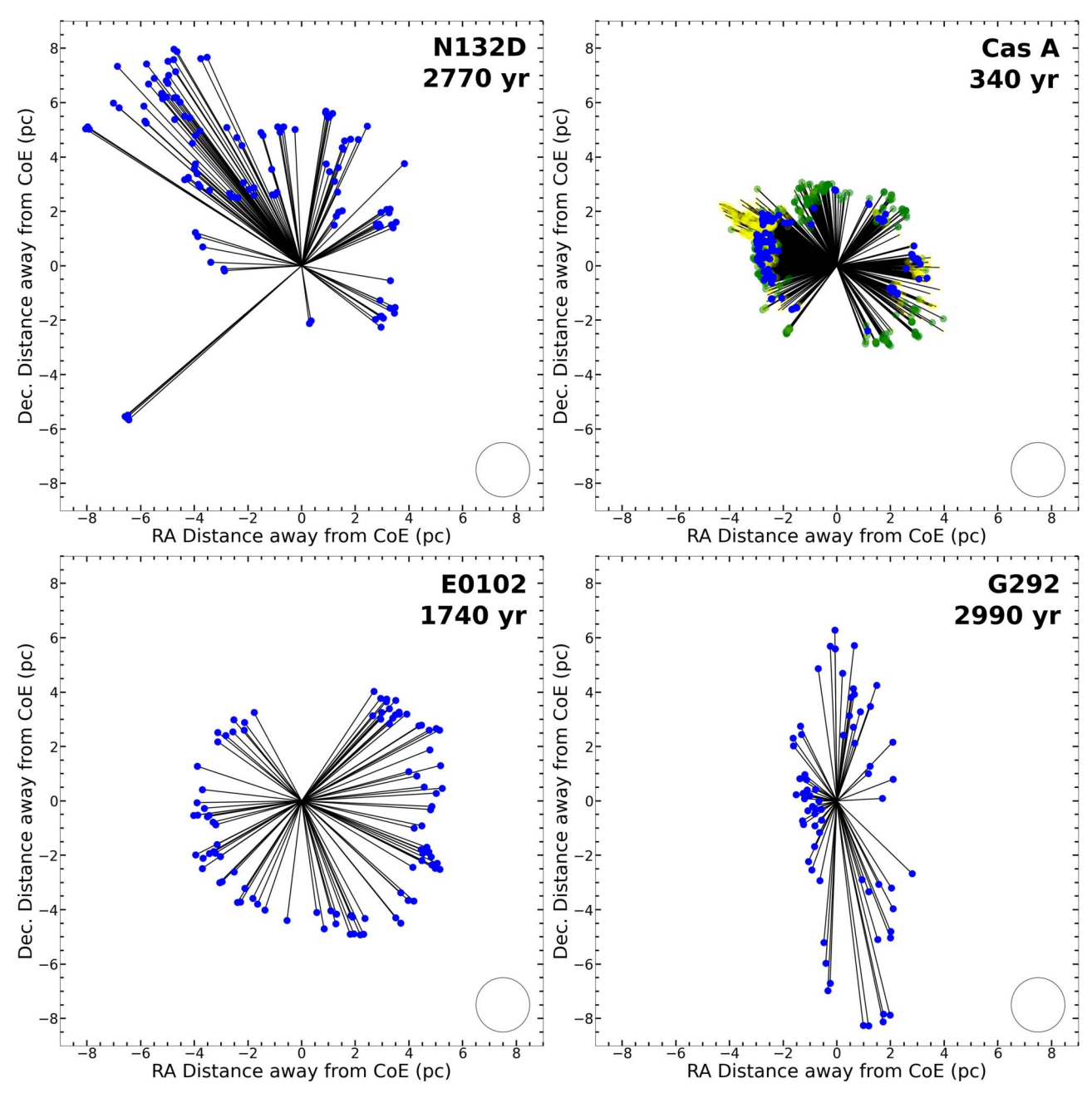


Figure 9. Locations of the O-rich knots (blue) of N132D (this work), E0102 (Banovetz et al. 2021), Cas A (Hammell & Fesen 2008), and G292 (Winkler et al. 2009), with trajectories (black) forced to originate on their proper motion-derived CoEs (Thorstensen et al. 2001; Winkler et al. 2009; Banovetz et al. 2021). Cas A also includes nitrogen-rich knots (green) and fast-moving knots (yellow; Hammell & Fesen 2008). The circle in the bottom right is 1 pc in radius. The physical distances were calculated using the distance estimates and CoEs from Table 2.

also evidence that G292's morphology is influenced by the motion of its surviving pulsar (Temim et al. 2022).

Cas A shows an asymmetry in the distribution of its highest-velocity oxygen knots, although not to the extent of N132D. This remnant shows a main shell of material moving at  $\approx 4000-6000~\rm km~s^{-1}$  that is broadly symmetric in the plane of the sky, but there is also an extended component of sulfur-rich material to the northeast that extends to velocities upwards of  $\approx 1.5 \times 10^4~\rm km~s^{-1}$  (Hammell & Fesen 2008; Fesen & Milisavljevic 2016). A complementary high-velocity outflow also exists in the southwest (Fesen 2001). Knots of other chemical abundances of Cas A are more symmetrical (see Fesen et al. 2006; Hammell & Fesen 2008; Milisavljevic & Fesen 2013), and although there is a gap of O-rich material in

the south of Cas A as seen in Figure 9, sulfur-rich main-shell ejecta at slower velocities are present. Simulations and observations of clumpy, filamentary nebulosities have shown that Cas A likely interacted with an inhomogenous CSM environment (Weil et al. 2020; Orlando et al. 2022). Overall, Cas A is a mixture of explosion asymmetry and an inhomogenous surrounding environment.

### 6. Conclusion

We present the first proper motion measurements of optically emitting ejecta of SNR N132D in the LMC. The proper motions were measured using manual and automated procedures applied to two epochs of high-resolution HST data taken

16 years apart with the same ACS/F475W instrument+filter combination sensitive to [O III]  $\lambda\lambda$ 4959, 5007 emission. With these proper motion measurements, we have increased the number of young, O-rich SNRs with proper motion-derived CoEs from three to four.

Our measurement of the CoE made via visual inspection converged on the coordinates  $\alpha = 5^{\rm h}25^{\rm m}01^{\rm s}71$   $\delta = -69^{\circ}38'$  41".64 (J2000) with a  $1\sigma$  uncertainty of 2".90. Our new CoE estimate is approximately 9".2 and 10".8 from previous estimates using geometric centers of emission (Morse et al. 1995). Combining this CoE estimate with the proper motion measurements leads to an age of  $2770 \pm 500$  yr, consistent with recent age estimates of  $\approx 2500$  yr by 3D reconstructions of N132D (Vogt & Dopita 2011; Law et al. 2020).

Our new CoE and explosion age serves as a useful guide for searches to locate the associated neutron star of the original core-collapse explosion of N132D (e.g., Holland-Ashford et al. 2017; Katsuda et al. 2018). To date, no neutron star has been identified in N132D, and our CoE identifies a region where a targeted search can be performed with new 1 Ms Chandra observations (PI: Plucinsky). Our CoE and age estimates of N132D can also effectively guide searches for a surviving binary companion to the progenitor system. To date, there have been no surviving stellar companions found for the population of nearby stripped-envelope SNRs (see, e.g., Kerzendorf et al. 2019). The nearby distance of N132D makes it possible to probe individual stars in the remnant's stellar neighborhood and avoid distance uncertainties and source confusion encountered in studies at extragalactic distances (Fox et al. 2022). An attempt was recently made to identify the surviving companion of E0102 (Li et al. 2021) using an updated CoE; thus our new CoE for N132D makes the remnant an excellent opportunity for a similar analysis.

We thank the anonymous referees and data editor for helping improving this paper. D.M. acknowledges NSF support from grants PHY-1914448, PHY- 2209451, AST-2037297, and AST-2206532. C.J.L. acknowledges funding from the National Science Foundation Graduate Research Fellowship under Grant DGE1745303. This research is based on observations made with the NASA/ESA Hubble Space Telescope obtained from the Space Telescope Science Institute, which is operated by the Association of Universities for Research in Astronomy, Inc., under NASA contract NAS 5-26555. These observations are associated with HST programs 6052, 12001, 12858, and 13378. Support for program #13378 was provided by NASA through a grant from the Space Telescope Science Institute, which is operated by the Association of Universities for Research in Astronomy, Inc., under NASA contract NAS 5-26555.

*Software:* PYRAF (Green 2012), ds9 (Smithsonian Astrophysical Observatory 2000), astrometry.net (Lang et al. 2010), Astropy (Astropy Collaboration et al. 2013, 2018).

# Appendix A A More Detailed Look into the Computer Vision Approach

### A.1. Previous Automation Techniques

In this paper, we used a new automated procedure for measuring the proper motions of SNR ejecta. Although manual inspection is a reliable method, using computer vision measurement techniques can allow for rapidly reproducible results, testing various quantitative thresholds, and scaling to a large number of proper motions more efficiently. One common technique is using a cross-correlation method (e.g., Currie et al. 1996), that has been used for the proper motion measurements of SNRs (e.g., Finkelstein et al. 2006; Winkler et al. 2009), stellar ejecta (e.g., Morse et al. 2001; Kiminki et al. 2016), and protostellar jets (e.g., Hartigan et al. 2001; Bally et al. 2002). This approach uses predefined box regions to outline a "clump" in one epoch that is then translated to a new position. The translated image is then subtracted by the second epoch and the translation that produces the minimum sum of the differences is the translation that is used. Other computer vision techniques for measuring proper motions in SNRs include measuring the optical flow, projection methods, and maximum likelihood functions (e.g., Borkowski et al. 2020).

The success of these procedures depends on the knots being bright and are best suited for large regions of gas. However, with the high spatial resolution of HST, we are able to resolve individual knots and cover more of the periphery of the SNR where faint, high proper motion ejecta knots are expected to be. Still, these knots can change in illumination and shape between epochs (e.g., Fesen et al. 2011; Patnaude & Fesen 2014), which can lead to errors in tracking. One of the goals of our new procedure is to be able to track fainter, individual knots for an older O-rich remnant such as N132D.

### A.2. Automated Proper Motion Measurement Procedure

### A.2.1. Image Preparation

The first step in the image preparation was to ensure that emission unrelated to N132D's O-rich material was corrected for and removed. Doing so ensured that our computer vision procedure only tracked [O III]  $\lambda\lambda4959$ , 5007 emission and was not confused by the CSM/ISM or stellar emission that was easily recognized in and avoided by the manually inspected proper motion measurements.

We first scaled the F550M (continuum) and F658N (H\$\alpha\$) images taken in 2004 to the ACS/F475W images by matching the flux of common stars and then subtracting the F550M and F658N emission from the ACS/F475W image. This was done to remove the stellar continuum and H\$\beta\$ emission (using H\$\alpha\$ as a tracer) from our images in order to track only the O-rich ejecta. We then manually removed any subtraction residuals outside of emission regions, and performed additional cleaning of the images using the cosmicray\_lacosmic task from the astropy package ccdproc.

## A.2.2. Identifying Knots

Next, small regions were identified for further individual processing. We chose regions that had strong oxygen emission or showed evidence of proper motion measurements when blinking between epochs. We divide these regions into 2" by 2" boxes, or stamps. Figure A1 shows all of the stamps while the first row of Figure A2 shows an enlarged example of a stamp. The stamp's size was chosen for its ability to encapsulate knot motion between epochs and to sample the local background. This is important since N132D's nonuniform emission properties makes using a global background value impractical. We allowed large overlap between the stamps to ensure that no knots were missed.

We then used the detect\_sources and deblend\_sources tasks from the photutils package in astropy to

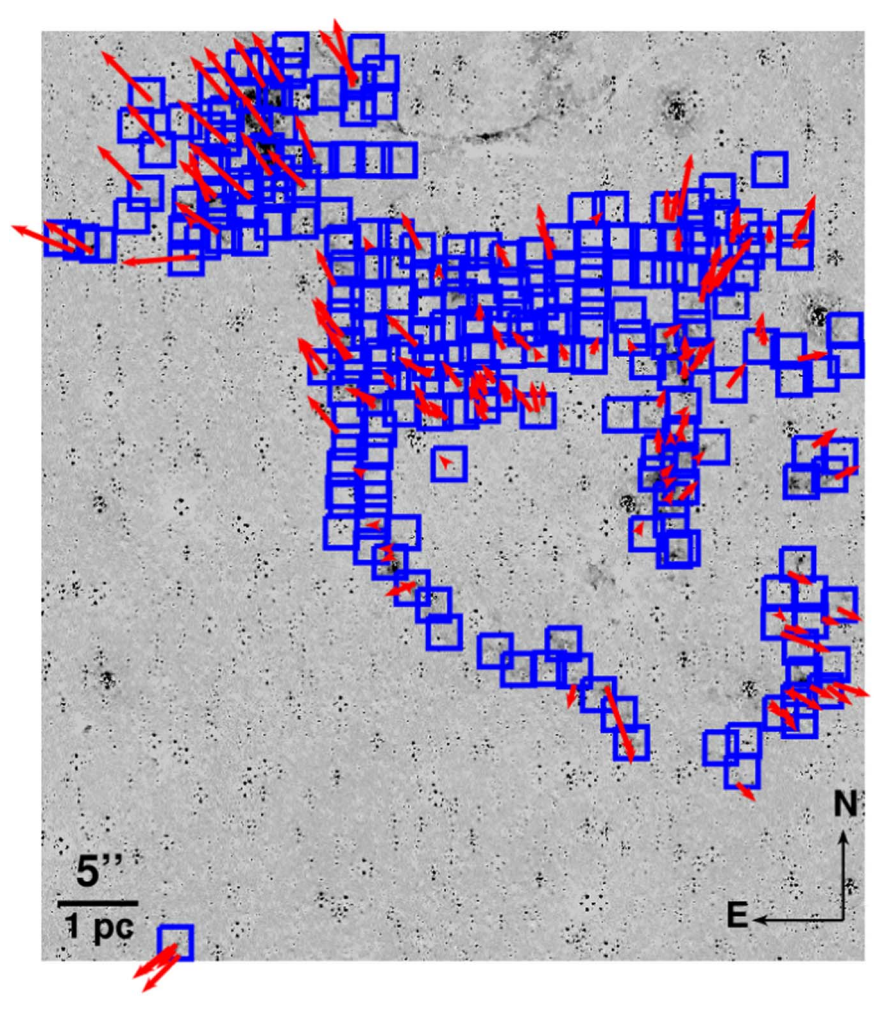


**Figure A1.** 2004 ACS/F475W continuum- and hydrogen-subtracted image with vectors representing the automated procedure's measured shifts (multiplied by a factor of 20 for visual clarity) shown in red. The stamps used in the automated procedure are shown as blue boxes. Empty boxes represent areas where the automated procedure could not detect any motion and/or identify knots.

identify knots, shown in the second and third row of Figure A2, respectively. Detect\_sources creates a segmented image which identifies sources of emission above a certain threshold. In our case, this was  $2\sigma$  above the median background of the 2'' by 2'' stamp. We further restricted our analysis to those knots containing emission that spanned at least four adjacent pixels. This pixel limit was selected to account for smaller, fainter knots than those found through visual inspection.

Deblend\_sources takes the segmented regions and finds the local maxima to separate potentially overlapping knots. For this process, we assumed a Gaussian kernel and a low contrast between the knots. We then apply three initial filters to remove any embedded residuals or hot pixels that were missed with cosmicray\_lacosmic. The first filter removes segments too close to the edges of the region, effectively reducing the region from 2" by 2" to 1."9 by 1."9. The next filter removes segments that do not move more than 1.5 mas yr<sup>-1</sup>, to remove any remaining residuals. This lower limit was chosen based on the manually inspected lowest proper motions around 3 mas yr<sup>-1</sup>. The last filter removes any segment that does not have a corresponding segment within 0."3 around it in the other epoch, to remove residuals or hot pixels that appear in one epoch but not the other.

### A.2.3. Matching Knots and Calculating Shifts

The changing brightness and shape of individual knots over time, in addition to any residual hot pixels, can affect the local peak position and the geometric center determined for each knot. To mitigate these effects, the local peaks in the identified knots are calculated using a KDE fit of the stamp (fourth row of Figure A2). To achieve sub-pixel accuracy, we found the best results by resampling the stamp from  $40 \times 40$  pixels to  $100 \times 100$  before applying the KDE, resulting in an error of 0.4 pixels ( $\approx 0.^{\prime\prime}.^{\prime\prime}.^{\prime\prime}.^{\prime\prime}.^{\prime\prime}$ ) for the calculated centers. We also found that the best bandwidth for the KDE was the the Silverman kernel (Silverman 1982) through manual inspection of the resulting KDE centers.

The next step is to match the knots between the epochs. Each pair of centroids is found using an initial guess of the CoE to find the position angle between the knot and the guess. We use the CoE calculated by the visually tracked knots for the initial guess. Each individual pair of knots between epochs is given a score, which is the shift between epochs multiplied by the difference between their trajectory and the position angle. The pair with the lowest score is selected as the correct combination. The combinations are then passed through two filters to mitigate outliers. Knot combinations are discarded if the difference between the trajectory and the position angle is

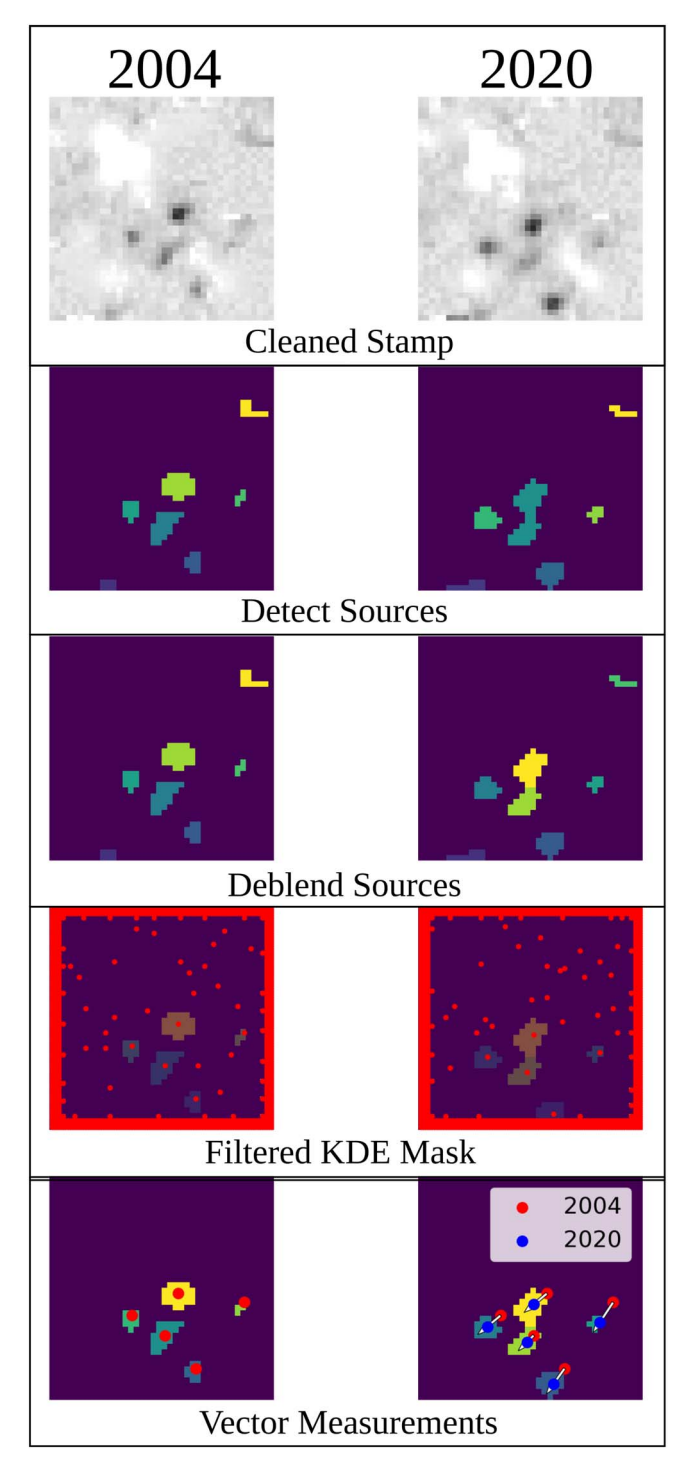


**Figure A2.** Steps needed for the computer vision technique to identify and measure the proper motions of ejecta knots. The 2004 and 2020 images of the same region as Figure 2 are shown on the left and right panels, respectively. The top row shows the original cutout of the continuum- and hydrogen-subtracted image in gray scale. The second and third rows show the results of the detect\_sources and deblend\_sources tasks, respectively. The fourth row shows the remaining segments after applying the KDE to the total region, identifying the localized peaks as shown in red. The final row shows the matched centroids. The centers are shown in red (2004) and blue (2020), with a white vector showing the motion between the two epochs.

greater than 90° and if the shift is larger than 30 mas yr<sup>-1</sup>, double the largest proper motion found using the visual measurements. The effect of changing these parameters are explored in Section 4. If multiple combinations use the same

endpoint (e.g., the deblending process splits a knot into two between epochs), the combination with the lowest score is chosen and the other is discarded. The final row of Figure A2 shows example final combinations.

Finally, we clip the top and bottom 5% of the proper motion vectors to remove outliers, average duplicate measurements due to overlapping stamps, and remove measurements that are within three pixels of the mask for subtraction residuals. The remaining measurements are used for the proper motion analysis as was done for the manual inspection in Section 3. We ensured that the procedure is robust using a toy model simulation, detailed in the following section.

### A.2.4. Simulated Proper Motion

We tested our procedure using a simulated, idealized SNR with ejecta moving ballisitically. We generated two 300 by 300 pixel images at a scale similar to HST with randomized background emission using the make\_noise\_image task in astropy's photutils package. The first was an image of 45 knots randomly placed to surround concentrically a test CoE located at the center of the image. The knots were drawn from a sample of the visually inspected HST knots, the majority of which were in the top third of knot brightness, and were placed using the geometric center of each knot. The second image was then created using a different randomized background and placing these knots certain distances radially away from the simulated CoE with proper motions following  $v \propto r$ . We implemented a scanning procedure to find regions containing the knots. This procedure scanned the image using subdivided regions to 40x40 pixel boxes with overlap between them. 15

Our automated procedure recovers all 45 knots. There was an average positional difference of 2.12 pixels ( $\approx$ 0."1 with HST resolution), an average shift difference of 1.53 pixels ( $\approx$ 3.5 mas yr<sup>-1</sup>), and an average angle difference of 0.12 radians between the inferred and true (simulated) values. We calculated a CoE of (154.77, 155.97) with a  $1\sigma$  error radius of 10.88 pixels ( $\approx$ 0."58) as compared to the simulated CoE of (150, 150). Overall, we were able to find all of the knots, match them correctly, and calculate their speeds and trajectories to return a CoE that is within  $1\sigma$  of the true value.

### A.3. Automated Procedure Results

This procedure was able to identify and track 137 knots of ejecta where the error of the proper motions was set to 0.4 pixels ( $\approx$ 0."2), from the sub-pixel ratio of the KDE. Figures A4–A7 show the knot locations, trajectories, and proper motion trends using this procedure. The procedure measured proper motions ranging from 2 to 17 mas yr<sup>-1</sup> and an *S* of 0."015 per km s<sup>-1</sup>.

Using the same CoE method as outlined in Section 3.1, the 137 proper motions yields a CoE of  $\alpha=5^{\rm h}25^{\rm m}02^{\rm s}.771$  and  $\delta=-69^{\circ}38'38''.985$  (J2000) with a  $1\sigma$  uncertainty of 4''.47. Figure A3 shows this result as compared to the other CoE estimates.

Utilizing this CoE and the proper motions, we calculate an age of  $3377 \pm 2241$  yr using all 137 knots, as shown in the left panel of Figure A5. This large discrepancy is most likely due to the procedure measuring the proper motions of artifacts or heavily decelerated knots, skewing the age estimates to higher

 $<sup>\</sup>overline{^{15}}$  We did not pass regions through the filters for hot pixels and star removal, as neither of these features were present in the simulated images.

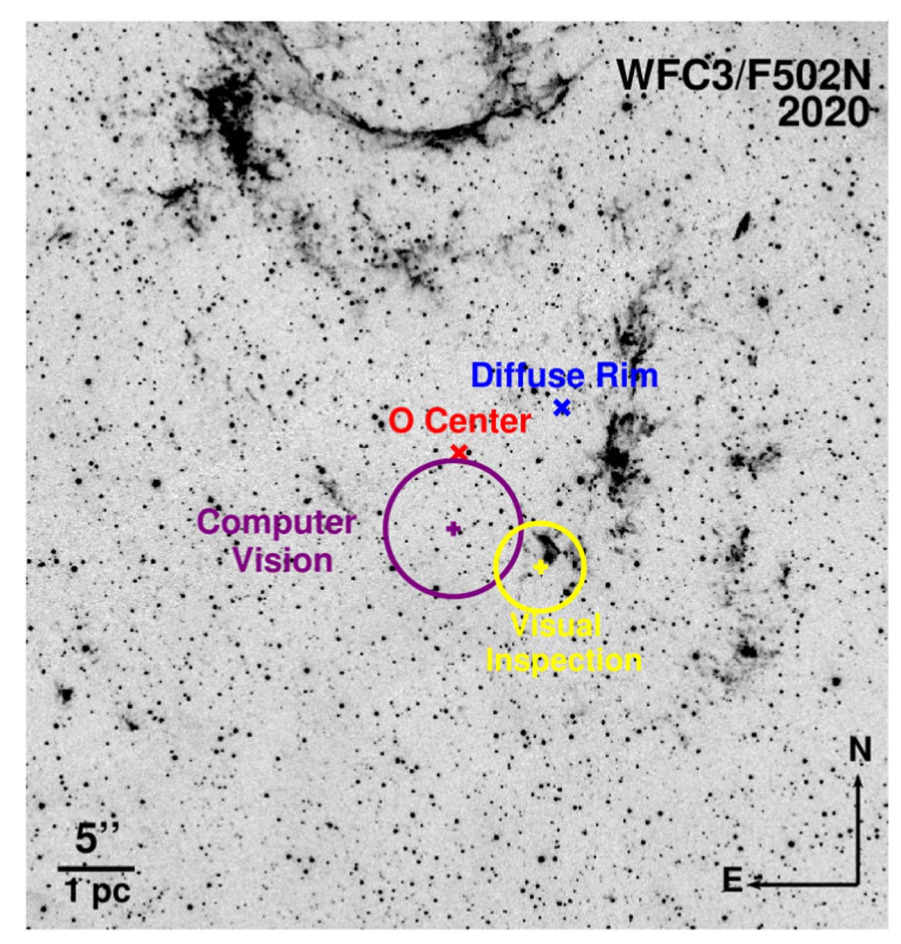


Figure A3. Similar to Figure 8 with the addition of the automated procedure's result of  $\alpha = 5^{\rm h}25^{\rm m}02^{\rm s}.771$  and  $\delta = -69^{\circ}38'38\rlap.''985$  (J2000) with a  $1\sigma$  uncertainty of  $4\rlap.''47$  in purple.

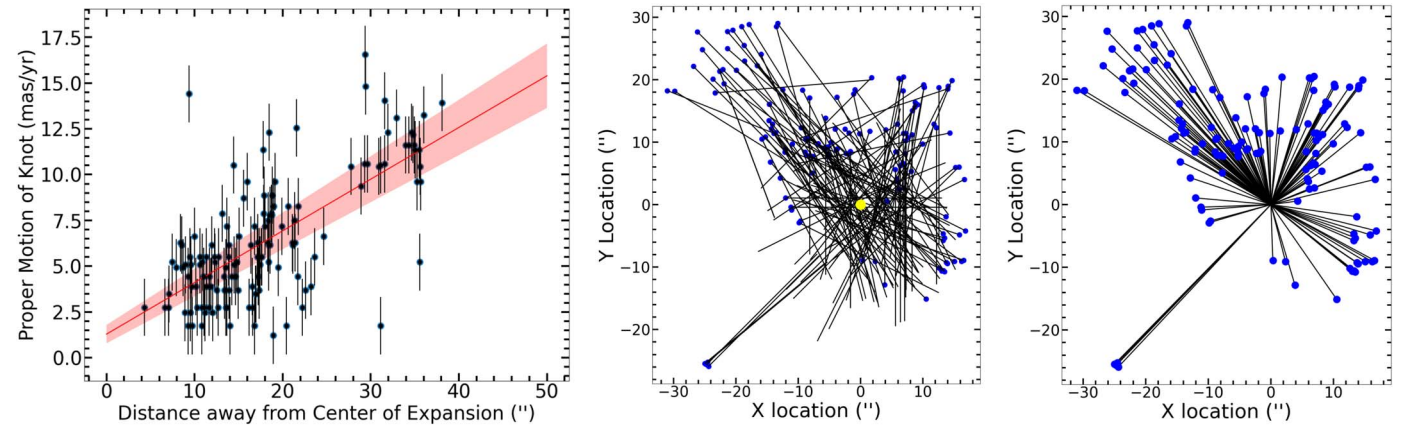


Figure A4. Similar to Figures 3 (left) and 5 (middle and right) but using the proper motions from the conservative parameters of the automated procedure.

values. To account for decelerated knots, we also calculated the age using knots above the median proper motion. These 70 knots yield an age of 2497  $\pm$  638 yr (right panel of Figure A5), much closer to that derived from the visually measured proper motions.

## A.4. Effect of Tuning Parameters

Figures A4, A3, and A5 show the results of using the conservative metrics to measure the proper motions, their trajectories, and subsequent CoE and explosion ages,

respectively. These results are highlighted in Section 4. The conservative parameter constraints used in the selection of knots adopted in our automated procedure were used to incorporate many degrees of freedom. However, the associated proper motion measurement uncertainties were much larger than those associated with our manual procedure. There are many ways that the parameters of knot selection can be further constrained to reduce the uncertainties and better match the manually measured CoE and age. We explored limiting the difference angle between the trajectory and position angle of the input CoE to 45° (from 90°),

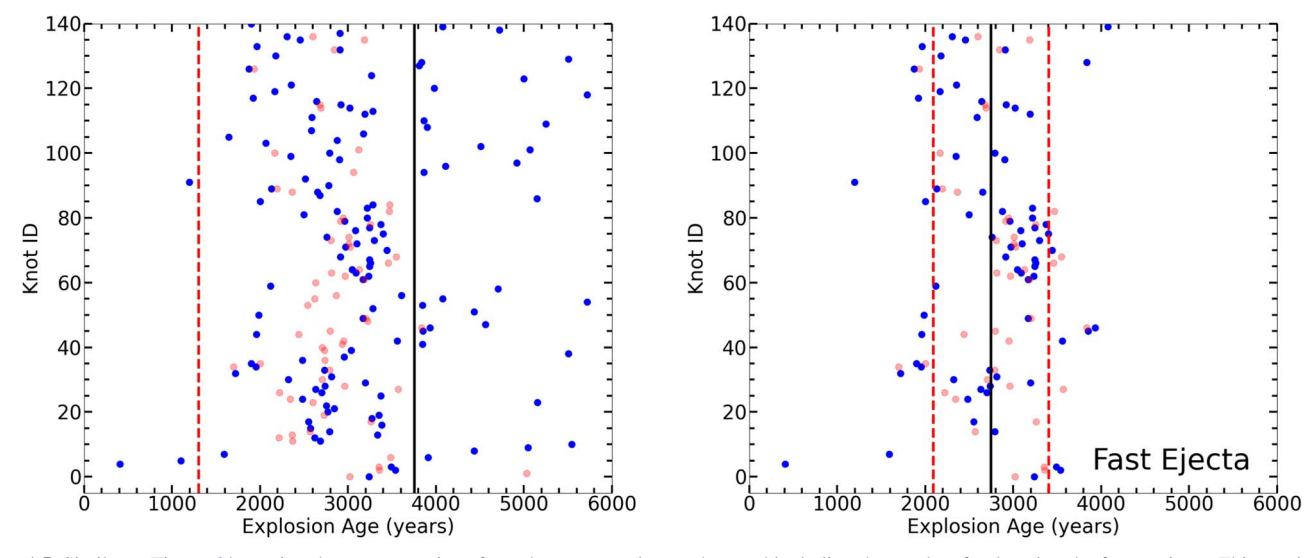


Figure A5. Similar to Figure 6 but using the proper motions from the automated procedure and including the results of only using the fastest ejecta. This results in an age of  $3377 \pm 2241$  yr using all the knots and  $2497 \pm 638$  yr using the fastest. The red shaded points correspond to the matching visually measured knots when applicable.

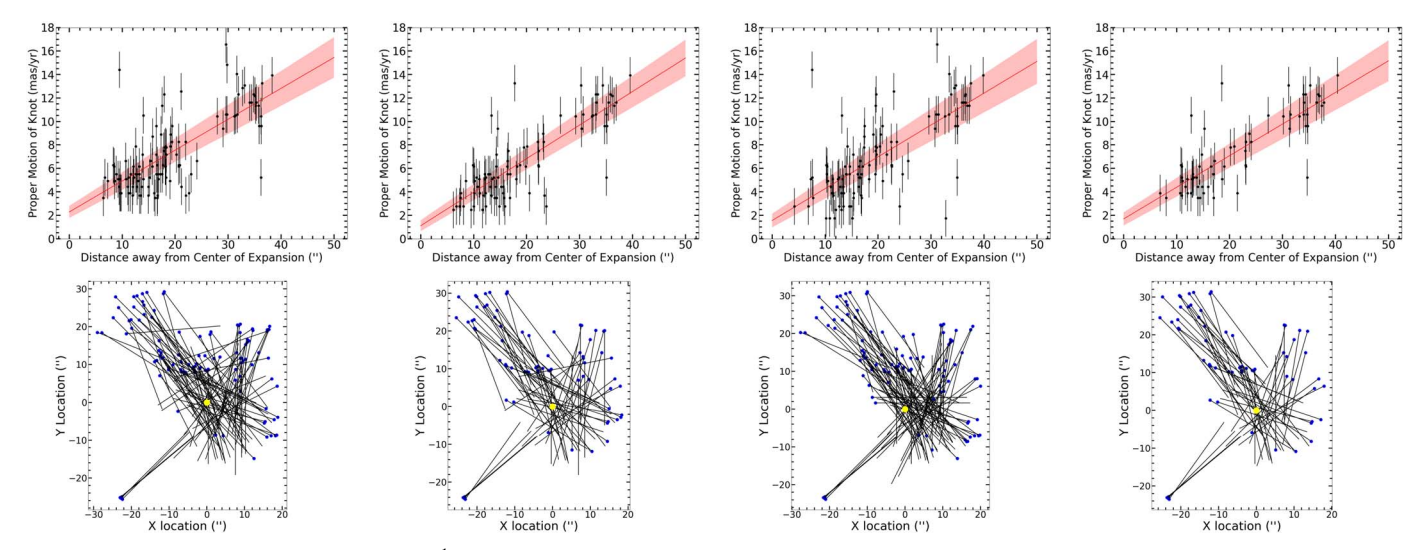


Figure A6. Similar to Figure A4 for the 3 mas yr<sup>-1</sup> lower limit (left), but increasing the brightness signal-to-noise ratio to  $3\sigma$  (middle left), reducing the trajectory and position angle difference of the knots to less than  $45^{\circ}$  (middle right), and applying all three variations (right).

increasing the minimum proper motion to 3 mas yr<sup>-1</sup> (from 1.5 mas yr<sup>-1</sup>), and using brighter knots by increasing the signal-to-noise ratio of the selected knots from  $2\sigma$  to  $3\sigma$ . We found that by tightening the boundaries of these parameters, the CoE of the automated procedure and the age calculation were both within  $1\sigma$  of the visual inspection results. The following section contains a detailed discussion about the effect of each of these parameters.

This procedure is ideal for an ejecta proper motion analysis of other SNRs. Two parameters that must be changed between SNRs are the KDE bandwidth and the arbitrary CoE. The KDE bandwidth is very sensitive and needs to be fine-tuned depending on the SNR. A bandwidth that is too small will identify many flux peaks within a knot while a bandwidth that is too large can miss fainter knots.

Another parameter that we explored was the influence of the choice of the arbitrary CoE for the trajectory versus the position angle cutoff. For our procedure outlined in Section A.2.3, we chose the CoE calculated using the visual inspection method.

Assuming this CoE was not available, we could have chosen the [O III] geometric center for our arbitrary CoE (Morse et al. 1995). We experimented with the  $45^{\circ}$  and  $90^{\circ}$  cutoffs with this arbitrary CoE and found that the resulting CoE did not match that found with the visually inspected CoE using an arbitrary initial CoE. However, we found that by iterating the arbitrary initial CoE calculation procedure, the CoE calculation converges to the same CoE as if using the visually inspected CoE for the arbitrary CoE. Running through 10 initial guess estimates of the CoE, we found that using a 45° cutoff would take 3-4 iterations, whereas the 90° cutoff would take two iterations before converging on the the same CoE as found by using the visual inspection CoE as the arbitrary CoE. As such, we would recommend anyone using our procedure to use the iteration method to verify their results, especially if using a geometric center for the arbitrary CoE, as they are often offset from the proper motion-derived centers (see Thorstensen et al. 2001; Katsuda et al. 2018; Banovetz et al. 2021).

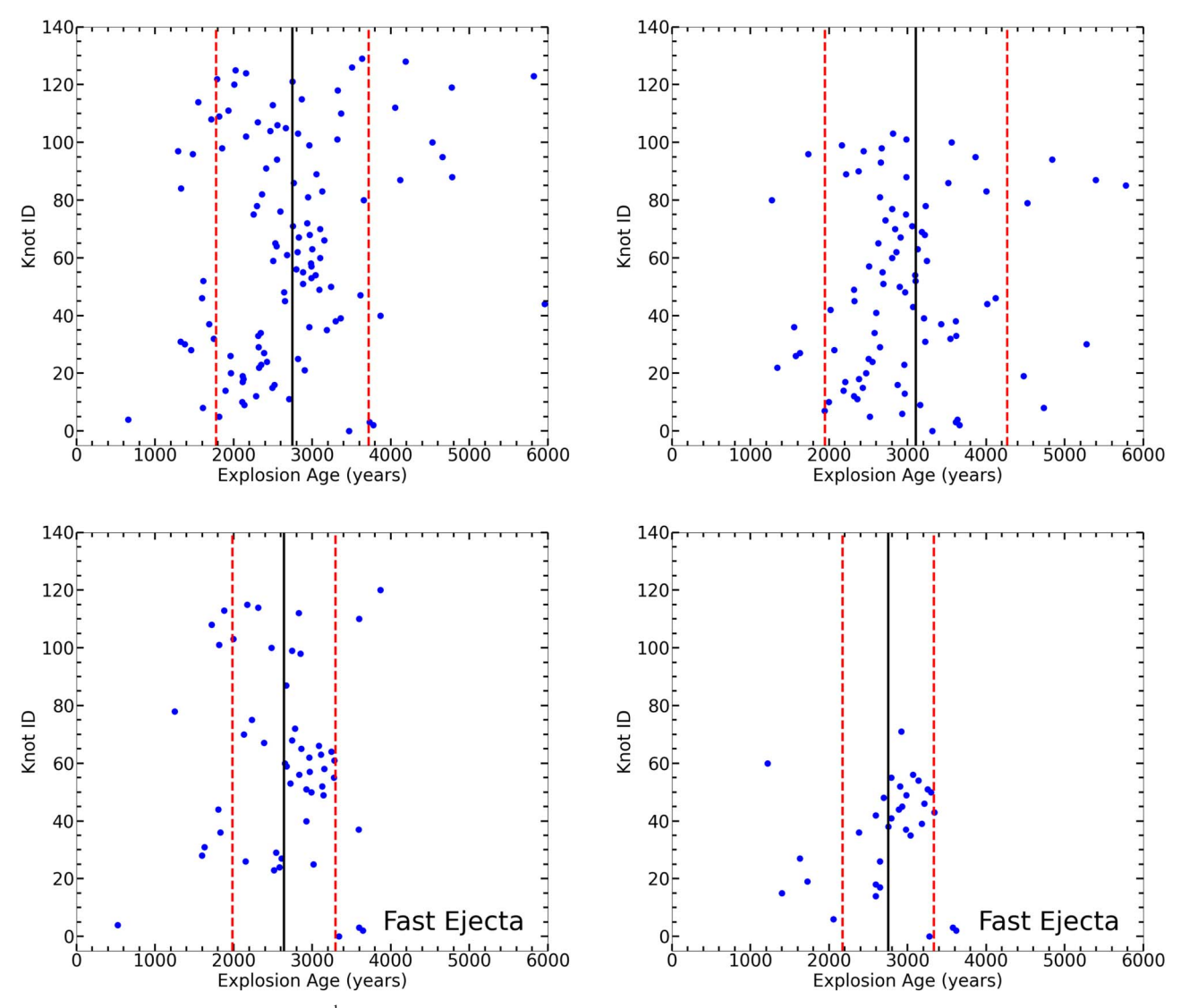


Figure A7. Similar to Figure 6 for the 3 mas yr<sup>-1</sup> lower limit (top left), but increasing the brightness signal-to-noise ratio to  $3\sigma$  (top right), considering a trajectory and position angle difference of the knots less than 45° (bottom left), and using all the parameters (bottom right) that match closest to the visual inspection result.

### A.4.1. Further Fine-tuning of Parameters

Here we discuss how measurements and calculations of the CoE and age are affected by the knot selection parameters in our automated procedure. Figure A4 shows the results of using the conservative parameters for the automated procedure. Figure A5 show the results of the age calculation when using all 137 knots, or only the fastest (70).

Figures A6 and A7 show the results of changing the parameters of the automated procedure. The left, middle left, middle right, and right panels show the effect of changing the parameters to incorporate a higher minimum speed (3 mas yr<sup>-1</sup>), only bright knots (3 $\sigma$ ), a trajectory and position angle difference of 45°, and all three of the changes, respectively.

## Appendix B Additional Tables

**Table A1**Anchor Star Coordinates

Star	R.A. (J2000)	Decl. (J2000)
1	5 <sup>h</sup> 24 <sup>m</sup> 53.87308	69 <sup>d</sup> 38 <sup>m</sup> 15 <sup>s</sup> 310
2	5 <sup>h</sup> 24 <sup>m</sup> 58 <sup>s</sup> 3686	69 <sup>d</sup> 38 <sup>m</sup> 35 <sup>s</sup> 298
3	5 <sup>h</sup> 24 <sup>m</sup> 57 <sup>s</sup> 8822	69 <sup>d</sup> 38 <sup>m</sup> 46 <sup>s</sup> 447
4	5 <sup>h</sup> 24 <sup>m</sup> 56 <sup>s</sup> .5386	69 <sup>d</sup> 39 <sup>m</sup> 38:340
5	$5^{\rm h}24^{\rm m}58^{\rm s}2838$	69 <sup>d</sup> 39 <sup>m</sup> 39 <sup>s</sup> 118
6	5 <sup>h</sup> 24 <sup>m</sup> 42 <sup>s</sup> 9113	69 <sup>d</sup> 39 <sup>m</sup> 13 <sup>s</sup> 996
7	5 <sup>h</sup> 24 <sup>m</sup> 47 <sup>s</sup> .0373	69 <sup>d</sup> 38 <sup>m</sup> 43 <sup>s</sup> 292
8	5 <sup>h</sup> 24 <sup>m</sup> 45 <sup>s</sup> .0608	69 <sup>d</sup> 38 <sup>m</sup> 41.8959
9	5 <sup>h</sup> 24 <sup>m</sup> 49 <sup>s</sup> .4502	69 <sup>d</sup> 38 <sup>m</sup> 29 <sup>s</sup> 224
10	5 <sup>h</sup> 25 <sup>m</sup> 04 <sup>s</sup> 9414	69 <sup>d</sup> 39 <sup>m</sup> 39 <sup>s</sup> 441
11	5 <sup>h</sup> 25 <sup>m</sup> 00 <sup>s</sup> .6230	69 <sup>d</sup> 38 <sup>m</sup> 00 <sup>s</sup> 893
12	5 <sup>h</sup> 24 <sup>m</sup> 51 <sup>s</sup> . 6282	69 <sup>d</sup> 39 <sup>m</sup> 05 <sup>s</sup> .757
13	5 <sup>h</sup> 24 <sup>m</sup> 49 <sup>s</sup> .5039	69 <sup>d</sup> 38 <sup>m</sup> 47 <sup>s</sup> 073
14	5 <sup>h</sup> 24 <sup>m</sup> 50 <sup>s</sup> .4438	69 <sup>d</sup> 39 <sup>m</sup> 48 <sup>s</sup> 192
15	5 <sup>h</sup> 24 <sup>m</sup> 52 <sup>s</sup> 2404	69 <sup>d</sup> 39 <sup>m</sup> 22.8696
16	5 <sup>h</sup> 25 <sup>m</sup> 01 <sup>s</sup> 3169	69 <sup>d</sup> 39 <sup>m</sup> 48 <sup>s</sup> .778
17	5 <sup>h</sup> 24 <sup>m</sup> 44 <sup>s</sup> .4366	69 <sup>d</sup> 39 <sup>m</sup> 09 <sup>s</sup> 882
18	5 <sup>h</sup> 24 <sup>m</sup> 56 <sup>s</sup> .5344	69 <sup>d</sup> 38 <sup>m</sup> 47 <sup>s</sup> 148
19	5 <sup>h</sup> 25 <sup>m</sup> 04 <sup>s</sup> .2141	69 <sup>d</sup> 40 <sup>m</sup> 09 <sup>s</sup> 653
20	5 <sup>h</sup> 24 <sup>m</sup> 58 <sup>s</sup> 9991	69 <sup>d</sup> 40 <sup>m</sup> 16 <sup>s</sup> .083
21	5 <sup>h</sup> 25 <sup>m</sup> 07 <sup>s</sup> 3918	69 <sup>d</sup> 40 <sup>m</sup> 02 s 308
22	5 <sup>h</sup> 25 <sup>m</sup> 06 <sup>s</sup> .7103	69 <sup>d</sup> 39 <sup>m</sup> 40: 337
23	5 <sup>h</sup> 25 <sup>m</sup> 11. <sup>s</sup> 2145	69 <sup>d</sup> 38 <sup>m</sup> 20 <sup>s</sup> 227
24	5 <sup>h</sup> 24 <sup>m</sup> 45 <sup>s</sup> .6713	69 <sup>d</sup> 38 <sup>m</sup> 35 <sup>s</sup> 164
25	5 <sup>h</sup> 24 <sup>m</sup> 47 <sup>s</sup> .2420	69 <sup>d</sup> 38 <sup>m</sup> 17 <sup>s</sup> 491
26	5 <sup>h</sup> 24 <sup>m</sup> 59 <sup>s</sup> .4994	69 <sup>d</sup> 40 <sup>m</sup> 08 <sup>s</sup> 583
27	5 <sup>h</sup> 25 <sup>m</sup> 08 <sup>s</sup> 2993	69 <sup>d</sup> 39 <sup>m</sup> 18 <sup>s</sup> 289
28	5 <sup>h</sup> 24 <sup>m</sup> 59 <sup>s</sup> .8352	69 <sup>d</sup> 40 <sup>m</sup> 17 <sup>s</sup> 268
29	5 <sup>h</sup> 24 <sup>m</sup> 49 <sup>s</sup> .7550	69 <sup>d</sup> 38 <sup>m</sup> 06 <sup>s</sup> 447
30	5 <sup>h</sup> 24 <sup>m</sup> 52 <sup>s</sup> .6476	69 <sup>d</sup> 38 <sup>m</sup> 01 s 440

 Table A2

 Manually Inspected Knot Measurements and Corresponding Automated Measurements

Knot	R.A.	Decl.		Visual	Procedure		Automated	Procedure
			$\mu_{lpha}$ .	$\sigma_{\!\mu_{lpha}}$ ,	$\mu_\delta$	$\sigma_{\!\mu_\delta}$ .	$\mu_{lpha}$	$\mu_{\delta}$ .
	(J2000)	(J2000)	(mas yr <sup>-1</sup> )	$(\text{mas yr}^{-1})$	$(\text{mas yr}^{-1})$	$(\text{mas yr}^{-1})$	(mas yr <sup>-1</sup> )	$(\text{mas yr}^{-1})$
1	5 <sup>h</sup> 25 <sup>m</sup> 06 <sup>s</sup> .759	69d39 <sup>m</sup> 04 <sup>s</sup> 815	-8.095	0.452	-7.722	0.431	-7.386	-7.386
2	5 <sup>h</sup> 25 <sup>m</sup> 06 <sup>s</sup> 817	69d39 <sup>m</sup> 04 <sup>s</sup> 523	-5.075	0.472	-4.399	0.409	-3.693	-3.693
3	5 <sup>h</sup> 25 <sup>m</sup> 06 <sup>s</sup> .791	69d39 <sup>m</sup> 04 s 138	-7.498	0.469	-6.602	0.413	-7.386	-6.155
4	5 <sup>h</sup> 25 <sup>m</sup> 06 <sup>s</sup> 870	69 <sup>d</sup> 39 <sup>m</sup> 04.341 s	-7.866	0.487	-6.336	0.392	-7.386	-6.155
5	5 <sup>h</sup> 24 <sup>m</sup> 58 <sup>s</sup> 937	69 <sup>d</sup> 38 <sup>m</sup> 48 <sup>s</sup> 660	5.251	0.571	-2.335	0.254	NA	NA
6	5 <sup>h</sup> 24 <sup>m</sup> 59 <sup>s</sup> 498	69 <sup>d</sup> 38 <sup>m</sup> 49 <sup>s</sup> 597	2.766	0.412	-3.161	0.470	2.462	-3.693
7	5 <sup>h</sup> 24 <sup>m</sup> 59 <sup>s</sup> 334	69 <sup>d</sup> 38 <sup>m</sup> 50 <sup>s</sup> . 789	3.786	0.403	-4.496	0.478	NA	NA
8	5 <sup>h</sup> 24 <sup>m</sup> 59 <sup>s</sup> 263	69 <sup>d</sup> 38 <sup>m</sup> 49 <sup>s</sup> 396	5.096	0.520	-3.409	0.347	NA	NA
9	5 <sup>h</sup> 24 <sup>m</sup> 59 <sup>s</sup> 365	69 <sup>d</sup> 38 <sup>m</sup> 49 <sup>s</sup> 148	5.557	0.543	-3.162	0.309	NA	NA
10	5 <sup>h</sup> 24 <sup>m</sup> 59 <sup>s</sup> 317	69 <sup>d</sup> 38 <sup>m</sup> 49 <sup>s</sup> 096	6.207	0.550	-3.349	0.297	NA	NA
11	5 <sup>h</sup> 24 <sup>m</sup> 59 <sup>s</sup> .068	69 <sup>d</sup> 38 <sup>m</sup> 47 <sup>s</sup> 891	5.977	0.555	-3.097	0.288	4.924	-3.693
12	5 <sup>h</sup> 24 <sup>m</sup> 58 <sup>s</sup> 914	69 <sup>d</sup> 38 <sup>m</sup> 47 <sup>s</sup> .797	7.006	0.578	-2.873	0.237	7.386	-2.462
13	5 <sup>h</sup> 24 <sup>m</sup> 59 <sup>s</sup> 357	69 <sup>d</sup> 38 <sup>m</sup> 46 <sup>s</sup> .738	6.259	0.589	-2.238	0.210	NA	NA
14	5 <sup>h</sup> 24 <sup>m</sup> 59 <sup>s</sup> .052	69 <sup>d</sup> 38 <sup>m</sup> 43 <sup>s</sup> .732	4.547	0.578	-1.877	0.238	3.693	-1.231
15	5 <sup>h</sup> 24 <sup>m</sup> 58 <sup>s</sup> 979	69 <sup>d</sup> 38 <sup>m</sup> 35 <sup>s</sup> .721	3.913	0.571	1.736	0.253	NA	NA
16	5 <sup>h</sup> 24 <sup>m</sup> 58 <sup>s</sup> 891	69 <sup>d</sup> 38 <sup>m</sup> 34 <sup>s</sup> 856	4.518	0.513	3.136	0.356	4.924	2.462
17	5 <sup>h</sup> 24 <sup>m</sup> 59 <sup>s</sup> .026	69 <sup>d</sup> 38 <sup>m</sup> 35 <sup>s</sup> 230	4.951	0.505	3.605	0.368	NA	NA
18	5 <sup>h</sup> 24 <sup>m</sup> 59 <sup>s</sup> .091	69 <sup>d</sup> 38 <sup>m</sup> 33 <sup>s</sup> 413	4.812	0.543	2.746	0.310	2.462	2.462
19	5 <sup>h</sup> 24 <sup>m</sup> 59 <sup>s</sup> 355	69 <sup>d</sup> 38 <sup>m</sup> 35 <sup>s</sup> 500	4.221	0.427	4.511	0.456	NA	NA
20	5 <sup>h</sup> 24 <sup>m</sup> 59 <sup>s</sup> 444	69 <sup>d</sup> 38 <sup>m</sup> 35 <sup>s</sup> 482	3.312	0.478	2.791	0.403	NA	NA
21	5 <sup>h</sup> 24 <sup>m</sup> 59 <sup>s</sup> 387	69 <sup>d</sup> 38 <sup>m</sup> 35 <sup>s</sup> 145	5.867	0.534	3.571	0.325	NA	NA

Table A2 (Continued)

Knot	R.A.	Decl.		Visual	Procedure		Automated	Procedure
	(J2000)	(J2000)	$\mu_{\alpha}$ (mas yr <sup>-1</sup> )	$( ext{mas yr}^{-1})$	$( ext{mas yr}^{\mu_\delta})$	$( ext{mas yr}^{\sigma_{\mu_{\delta}}})$	$\mu_{\alpha}$ (mas yr <sup>-1</sup> )	$( ext{mas yr}^{-1})$
22	5 <sup>h</sup> 24 <sup>m</sup> 59 <sup>s</sup> .471	69 <sup>d</sup> 38 <sup>m</sup> 35 <sup>s</sup> 149	3.199	0.407	3.728	0.474	NA	NA
23	5 <sup>h</sup> 24 <sup>m</sup> 59 <sup>s</sup> 061	69 <sup>d</sup> 38 <sup>m</sup> 32 <sup>s</sup> 842	3.358	0.462	3.061	0.421	2.462	2.462
24	5 <sup>h</sup> 24 <sup>m</sup> 59 <sup>s</sup> 165	69 <sup>d</sup> 38 <sup>m</sup> 32 <sup>s</sup> 899	6.936	0.545	3.905	0.307	4.924	3.693
25	5 <sup>h</sup> 24 <sup>m</sup> 59 <sup>s</sup> 336	69 <sup>d</sup> 38 <sup>m</sup> 33 <sup>s</sup> 396	5.870	0.548	3.218	0.300	NA	NA
26	5 <sup>h</sup> 25 <sup>m</sup> 00 <sup>s</sup> 580	69 <sup>d</sup> 38 <sup>m</sup> 33 <sup>s</sup> 323	1.729	0.248	4.002	0.574	1.231	1.231
27	5 <sup>h</sup> 25 <sup>m</sup> 00 <sup>s</sup> 657	69 <sup>d</sup> 38 <sup>m</sup> 33 § 912	1.930	0.281	3.832	0.558	NA	NA
28	5 <sup>h</sup> 25 <sup>m</sup> 00 <sup>s</sup> 707	69 <sup>d</sup> 38 <sup>m</sup> 35 <sup>s</sup> 283	2.645	0.433	2.750	0.451	NA	NA
29	5 <sup>h</sup> 25 <sup>m</sup> 00 <sup>s</sup> 614	69 <sup>d</sup> 38 <sup>m</sup> 30 <sup>s</sup> 296	2.558	0.324	4.227	0.535	NA	NA
30	5 <sup>h</sup> 25 <sup>m</sup> 00 <sup>s</sup> 476	69 <sup>d</sup> 38 <sup>m</sup> 33 <sup>s</sup> 102	1.871	0.244	4.407	0.575	NA	NA
31	5 <sup>h</sup> 25 <sup>m</sup> 00 <sup>s</sup> . 700	69 <sup>d</sup> 38 <sup>m</sup> 28 <sup>s</sup> 663	0.142	0.015	5.776	0.625	0.000	3.693
32	5 <sup>h</sup> 25 <sup>m</sup> 00 <sup>s</sup> 845	69 <sup>d</sup> 38 <sup>m</sup> 27 <sup>s</sup> 202	2.276	0.252	5.171	0.572	3.693	2.462
33	5 <sup>h</sup> 25 <sup>m</sup> 00 <sup>s</sup> 594	69 <sup>d</sup> 38 <sup>m</sup> 26 <sup>s</sup> 570	1.869	0.145	7.859	0.608	NA	NA
34	5 <sup>h</sup> 25 <sup>m</sup> 00 <sup>s</sup> 948	69 <sup>d</sup> 38 <sup>m</sup> 26 <sup>s</sup> .000	2.112	0.195	6.414	0.594	3.693 0	2.462
35	5 <sup>h</sup> 25 <sup>m</sup> 00 <sup>s</sup> .447	69 <sup>d</sup> 38 <sup>m</sup> 23 <sup>s</sup> .793	1.778	0.177	6.031	0.599	1.231	6.155
36	5 <sup>h</sup> 25 <sup>m</sup> 00 <sup>s</sup> 407	69 <sup>d</sup> 38 <sup>m</sup> 22 <sup>s</sup> 524	1.459	0.119	7.525	0.614	2.462	7.386
37	5 <sup>h</sup> 25 <sup>m</sup> 00 <sup>s</sup> 231	69 <sup>d</sup> 38 <sup>m</sup> 22 <sup>s</sup> 238	2.345	0.183	7.649	0.598	NA	NA
38	5 <sup>h</sup> 25 <sup>m</sup> 00 <sup>s</sup> .473	69 <sup>d</sup> 38 <sup>m</sup> 23 <sup>s</sup> 509	3.180	0.264	6.810	0.566	4.924	7.386
39	5 <sup>h</sup> 24 <sup>m</sup> 59 <sup>s</sup> .998	69 <sup>d</sup> 38 <sup>m</sup> 22 <sup>s</sup> 286	2.610	0.237	6.370	0.578	NA	NA
40	5 <sup>h</sup> 25 <sup>m</sup> 00 <sup>s</sup> 851	69 <sup>d</sup> 38 <sup>m</sup> 18 <sup>s</sup> .795	1.378	0.099	8.562	0.617	1.231	6.155
41	5 <sup>h</sup> 25 <sup>m</sup> 00 <sup>s</sup> .920	69 <sup>d</sup> 38 <sup>m</sup> 18.666	2.360	0.233	5.875	0.580	0.000	6.155
42	5 <sup>h</sup> 25 <sup>m</sup> 00 <sup>s</sup> .956	69 <sup>d</sup> 38 <sup>m</sup> 17 <sup>s</sup> 995	0.808	0.056	8.964	0.622	NA	NA
43	5 <sup>h</sup> 25 <sup>m</sup> 00 <sup>s</sup> 964	69 <sup>d</sup> 38 <sup>m</sup> 18 <sup>s</sup> 212	1.658	0.138	7.308	0.610	0.000	6.155
44	5 <sup>h</sup> 25 <sup>m</sup> 00 <sup>s</sup> .764	69 <sup>d</sup> 38 <sup>m</sup> 18 <sup>s</sup> 370	1.616	0.099	10.030	0.617	2.462	12.311
45	5 <sup>h</sup> 25 <sup>m</sup> 00 <sup>s</sup> 892	69 <sup>d</sup> 38 <sup>m</sup> 18 <sup>s</sup> 986	1.431	0.113	7.782	0.615	1.231	6.155
46	5 <sup>h</sup> 25 <sup>m</sup> 01 <sup>s</sup> 869	69 <sup>d</sup> 38 <sup>m</sup> 20 <sup>s</sup> . 792	-1.263	0.074	10.628	0.621	NA	NA
47	5 <sup>h</sup> 25 <sup>m</sup> 02 <sup>s</sup> 200	69 <sup>d</sup> 38 <sup>m</sup> 20 <sup>s</sup> 383	-1.787	0.150	7.249	0.607	-3.693	4.924
48	5 <sup>h</sup> 25 <sup>m</sup> 02 s 373	69 <sup>d</sup> 38 <sup>m</sup> 20 <sup>s</sup> 365	-2.316	0.191	7.216	0.595	-3.693	4.924
49	5 <sup>h</sup> 25 <sup>m</sup> 02 <sup>s</sup> 258	69 <sup>d</sup> 38 <sup>m</sup> 20 <sup>s</sup> 524	-2.631	0.187	8.404	0.596	-3.693	4.924
50	5 <sup>h</sup> 25 <sup>m</sup> 02 s 309	69 <sup>d</sup> 38 <sup>m</sup> 21 <sup>s</sup> 170	-1.858	0.105	10.877	0.616	-2.462	11.080
51	5 <sup>h</sup> 25 <sup>m</sup> 02 <sup>s</sup> 559 5 <sup>h</sup> 25 <sup>m</sup> 02 <sup>s</sup> 397	69 <sup>d</sup> 38 <sup>m</sup> 26 <sup>s</sup> 825	-3.684	0.396	4.500	0.484	-3.693	3.693
52	5 <sup>h</sup> 25 <sup>m</sup> 02; 397 5 <sup>h</sup> 25 <sup>m</sup> 02; 455	69 <sup>d</sup> 38 <sup>m</sup> 30 <sup>s</sup> 352 69 <sup>d</sup> 38 <sup>m</sup> 30 <sup>s</sup> 719	-1.014	0.141	4.365	0.609	0.000	4.924
53 54	5 25 02:455 5 <sup>h</sup> 25 <sup>m</sup> 02:538	69 <sup>d</sup> 38 <sup>m</sup> 30 <sup>s</sup> .703	-1.352 $-4.625$	0.141 0.405	5.836 5.428	0.609 0.476	-1.231 $-3.693$	6.155 4.924
55	5 25 02:338 5h25m03:081	69 <sup>d</sup> 38 <sup>m</sup> 30 <sup>s</sup> .761	-4.623 -2.899	0.403	3.830	0.478	-3.093 -1.231	3.693
56	5 <sup>h</sup> 25 <sup>m</sup> 03 <sup>s</sup> .079	69 <sup>d</sup> 38 <sup>m</sup> 29 <sup>s</sup> 633	-2.899 $-2.074$	0.300	3.791	0.498	-1.231 $-2.462$	3.093 4.924
57	5 <sup>h</sup> 25 <sup>m</sup> 03 <sup>s</sup> 225	69 38 29.033 69 <sup>d</sup> 38 <sup>m</sup> 29.853	-2.074 $-4.040$	0.461	3.700	0.422	-2.462 $-1.231$	2.462
58	5 <sup>h</sup> 25 <sup>m</sup> 03.387	69 <sup>d</sup> 38 <sup>m</sup> 28 <sup>s</sup> 857	-2.748	0.259	6.035	0.569	-3.693	4.924
59	5 <sup>h</sup> 25 <sup>m</sup> 03.553	69 <sup>d</sup> 38 <sup>m</sup> 31 <sup>s</sup> 191	-2.748 $-4.421$	0.466	3.954	0.417	-3.693 -3.693	3.693
60	5 <sup>h</sup> 25 <sup>m</sup> 03 <sup>s</sup> 644	69 <sup>d</sup> 38 <sup>m</sup> 31 <sup>s</sup> 047	-4.108	0.393	5.077	0.486	-4.924	2.462
61	5 <sup>h</sup> 25 <sup>m</sup> 03 <sup>s</sup> 738	69 <sup>d</sup> 38 <sup>m</sup> 30 <sup>s</sup> 971	-4.446	0.443	4.420	0.441	-2.462	3.693
62	5 <sup>h</sup> 25 <sup>m</sup> 03 <sup>s</sup> 792	69 <sup>d</sup> 38 <sup>m</sup> 30 <sup>s</sup> 488	-3.843	0.400	4.604	0.480	-2.462	4.924
63	5 <sup>h</sup> 25 <sup>m</sup> 04 <sup>s</sup> .737	69 <sup>d</sup> 38 <sup>m</sup> 37 <sup>s</sup> 017	-4.387	0.599	1.320	0.180	NA	NA
64	5 <sup>h</sup> 25 <sup>m</sup> 04.584	69 <sup>d</sup> 38 <sup>m</sup> 38 <sup>s</sup> 620	-7.044	0.540	4.111	0.315	NA	NA
65	5 <sup>h</sup> 25 <sup>m</sup> 04 <sup>s</sup> 800	69 <sup>d</sup> 38 <sup>m</sup> 36.432	-6.623	0.483	5.433	0.396	NA	NA
66	5 <sup>h</sup> 25 <sup>m</sup> 03 § 965	69 <sup>d</sup> 38 <sup>m</sup> 41 <sup>s</sup> 964	-2.947	0.602	0.823	0.168	-2.462	1.231
67	5 <sup>h</sup> 25 <sup>m</sup> 04 s 343	69 <sup>d</sup> 38 <sup>m</sup> 40 <sup>s</sup> 948	-4.563	0.553	2.407	0.292	NA	NA
68	5h25m03 s 941	69 <sup>d</sup> 38 <sup>m</sup> 42 <sup>s</sup> 226	-5.002	0.622	0.481	0.060	-2.462	1.231
69	5 <sup>h</sup> 25 <sup>m</sup> 04 <sup>s</sup> 387	69 <sup>d</sup> 38 <sup>m</sup> 30 <sup>s</sup> 020	-5.281	0.410	6.064	0.471	-6.155	2.462
70	5 <sup>h</sup> 25 <sup>m</sup> 04 <sup>s</sup> 664	69 <sup>d</sup> 38 <sup>m</sup> 29 <sup>s</sup> 489	-5.792	0.441	5.809	0.443	NA	NA
71	5h25m04 s 712	69 <sup>d</sup> 38 <sup>m</sup> 29 <sup>s</sup> 118	-5.238	0.465	4.714	0.418	NA	NA
72	5 <sup>h</sup> 25 <sup>m</sup> 05 <sup>s</sup> 020	69 <sup>d</sup> 38 <sup>m</sup> 28 <sup>s</sup> 243	-5.438	0.469	4.799	0.414	-4.924	6.155
73	5 <sup>h</sup> 25 <sup>m</sup> 05 <sup>s</sup> 009	69 <sup>d</sup> 38 <sup>m</sup> 28 <sup>s</sup> 027	-4.951	0.417	5.517	0.465	-4.924	6.155
74	5 <sup>h</sup> 25 <sup>m</sup> 04 <sup>s</sup> .751	$69^{d}38^{m}27^{s}.468$	-4.284	0.342	6.548	0.523	-3.693	6.155
75	$5^{h}25^{m}05^{s}.117$	$69^{d}38^{m}28^{s}383$	-3.508	0.360	4.986	0.511	-3.693	7.386
76	5 <sup>h</sup> 25 <sup>m</sup> 04 <sup>s</sup> 831	69 <sup>d</sup> 38 <sup>m</sup> 26 <sup>s</sup> .683	-4.528	0.413	5.136	0.469	-4.924	7.386
77	5 <sup>h</sup> 25 <sup>m</sup> 04 <sup>s</sup> .797	$69^{d}38^{m}26\stackrel{s}{.}002$	-5.496	0.402	6.537	0.478	-6.155	7.386
78	5 <sup>h</sup> 25 <sup>m</sup> 02 <sup>s</sup> 870	$69^{d}38^{m}21\stackrel{s}{.}258$	-3.230	0.273	6.654	0.562	-2.462	4.924
79	5 <sup>h</sup> 25 <sup>m</sup> 02 <sup>s</sup> 811	$69^{d}38^{m}21\stackrel{s}{.}684$	-5.987	0.404	7.064	0.477	-2.462	4.924
80	5 <sup>h</sup> 25 <sup>m</sup> 03 <sup>s</sup> 575	69 <sup>d</sup> 38 <sup>m</sup> 22 s 023	-3.531	0.270	7.370	0.564	0.000	1.231
81	5 <sup>h</sup> 25 <sup>m</sup> 03 <sup>s</sup> 874	69 <sup>d</sup> 38 <sup>m</sup> 20 <sup>s</sup> 501	-3.165	0.291	6.015	0.553	-3.693	7.386
82	5 <sup>h</sup> 25 <sup>m</sup> 03 <sup>s</sup> 436	69 <sup>d</sup> 38 <sup>m</sup> 23 <sup>s</sup> 201	-2.373	0.198	7.098	0.593	NA	NA
83	5 <sup>h</sup> 25 <sup>m</sup> 04 <sup>s</sup> 893	69 <sup>d</sup> 38 <sup>m</sup> 22 <sup>s</sup> 848	-4.533	0.306	8.081	0.545	-3.693	7.386

Table A2 (Continued)

Knot	R.A.	Decl.		Visual	Procedure		Automated	Procedure
	(J2000)	(J2000)	$\mu_{lpha}$ (mas yr $^{-1}$ )	$( ext{mas yr}^{\sigma_{\mu_{lpha}}})$	$( ext{mas yr}^{-1})$	$( ext{mas yr}^{\sigma_{\mu_{\delta}}})$	$\mu_{lpha}$ (mas yr $^{-1}$ )	$( ext{mas yr}^{\mu_{\delta}})$
84	5 <sup>h</sup> 25 <sup>m</sup> 04 <sup>s</sup> 797	69 <sup>d</sup> 38 <sup>m</sup> 21 <sup>s</sup> .717	-7.334	0.410	8.452	0.472	NA	NA
85	5 <sup>h</sup> 25 <sup>m</sup> 04 <sup>s</sup> 663	69 <sup>d</sup> 38 <sup>m</sup> 20 <sup>s</sup> 967	-7.508	0.428	7.979	0.455	NA	NA
86	5 <sup>h</sup> 25 <sup>m</sup> 04 <sup>s</sup> 954	69 <sup>d</sup> 38 <sup>m</sup> 18 <sup>s</sup> 989	-5.288	0.281	10.497	0.558	NA	NA
87	5 <sup>h</sup> 25 <sup>m</sup> 05 <sup>s</sup> 116	69 <sup>d</sup> 38 <sup>m</sup> 18 <sup>s</sup> .782	-6.096	0.363	8.557	0.509	NA	NA
88	5 <sup>h</sup> 25 <sup>m</sup> 05 <sup>s</sup> 411	69 <sup>d</sup> 38 <sup>m</sup> 19 <sup>s</sup> 262	-7.661	0.502	5.670	0.372	NA	NA
89	5h25m08:036	69 <sup>d</sup> 38 <sup>m</sup> 20 <sup>s</sup> 676	-11.101	0.512	7.791	0.359	-12.311	4.924
90	5 <sup>h</sup> 25 <sup>m</sup> 07 <sup>s</sup> .979	69 <sup>d</sup> 38 <sup>m</sup> 20 <sup>s</sup> 386	-10.437	0.505	7.603	0.368	-12.311	4.924
91	5h25m07 s 921	69 <sup>d</sup> 38 <sup>m</sup> 20 <sup>s</sup> .738	-8.091	0.394	9.951	0.485	-9.848	6.155
92	$5^{h}25^{m}07 \stackrel{s}{.} 220$	69 <sup>d</sup> 38 <sup>m</sup> 16 <sup>s</sup> .762	-9.750	0.454	9.215	0.429	-8.617	8.617
93	5 <sup>h</sup> 25 <sup>m</sup> 07 <sup>s</sup> .046	69 <sup>d</sup> 38 <sup>m</sup> 17 <sup>s</sup> 499	-10.700	0.463	9.720	0.420	NA	NA
94	5h25m06 s 250	69 <sup>d</sup> 38 <sup>m</sup> 19 <sup>s</sup> 801	-8.183	0.501	6.116	0.374	-8.617	6.155
95	5 <sup>h</sup> 25 <sup>m</sup> 06 <sup>s</sup> 290	69 <sup>d</sup> 38 <sup>m</sup> 19 <sup>s</sup> 507	-8.475	0.492	6.644	0.386	-8.617	6.155
96	5 <sup>h</sup> 25 <sup>m</sup> 06 <sup>s</sup> 317	69 <sup>d</sup> 38 <sup>m</sup> 17 <sup>s</sup> 245	-6.808	0.433	7.101	0.451	-7.386	7.386
97	5h25m05 s 259	69 <sup>d</sup> 38 <sup>m</sup> 16 <sup>s</sup> 604	-6.608	0.401	7.889	0.479	-7.386	7.386
98	5h25m05 8423	69 <sup>d</sup> 38 <sup>m</sup> 15 <sup>s</sup> 945	-5.608	0.298	10.350	0.550	NA	NA
99	5 <sup>h</sup> 25 <sup>m</sup> 05:352	69 <sup>d</sup> 38 <sup>m</sup> 15 <sup>s</sup> 983	-6.149	0.357	8.852	0.513	NA	NA
100	5 <sup>h</sup> 25 <sup>m</sup> 05 <sup>s</sup> 648	69 <sup>d</sup> 38 <sup>m</sup> 15 <sup>s</sup> 853	-6.412	0.367	8.849	0.506	-6.155	8.617
101	5 <sup>h</sup> 25 <sup>m</sup> 05 <sup>s</sup> .767	69 <sup>d</sup> 38 <sup>m</sup> 16 <sup>s</sup> 143	-6.894	0.343	10.506	0.523	-6.155	8.617
102	5 <sup>h</sup> 25 <sup>m</sup> 05 <sup>s</sup> .794	69 <sup>d</sup> 38 <sup>m</sup> 15 <sup>s</sup> 290	-6.897	0.366	9.563	0.507	NA	NA
103	5 <sup>h</sup> 25 <sup>m</sup> 06 <sup>s</sup> 181	69 <sup>d</sup> 38 <sup>m</sup> 13 <sup>s</sup> 869	-7.882	0.410	9.053	0.471	-9.848	8.617
104	5 <sup>h</sup> 25 <sup>m</sup> 05 <sup>s</sup> 608	69 <sup>d</sup> 38 <sup>m</sup> 13 <sup>s</sup> .780	-6.183	0.314	10.619	0.540	-6.155	8.617
105	5h25m06 s 015	69 <sup>d</sup> 38 <sup>m</sup> 13 <sup>s</sup> .013	-8.498	0.391	10.610	0.488	NA	NA
106	5 <sup>h</sup> 25 <sup>m</sup> 05 <sup>s</sup> 661	69 <sup>d</sup> 38 <sup>m</sup> 13 <sup>s</sup> 407	-6.182	0.323	10.241	0.535	-6.155	8.617
107	5h25m05 s 593	69 <sup>d</sup> 38 <sup>m</sup> 12 <sup>s</sup> 558	-6.322	0.313	10.925	0.541	NA	NA
108	5 <sup>h</sup> 25 <sup>m</sup> 07 <sup>s</sup> .099	69 <sup>d</sup> 38 <sup>m</sup> 11. <sup>s</sup> 216	-9.856	0.435	10.153	0.448	-9.848	9.848
109	5 <sup>h</sup> 25 <sup>m</sup> 06 <sup>s</sup> 241	69 <sup>d</sup> 38 <sup>m</sup> 10 <sup>s</sup> 852	-7.146	0.375	9.535	0.500	-7.386	8.617
110	5h25m05 s 609	69 <sup>d</sup> 38 <sup>m</sup> 10 <sup>s</sup> 424	-7.850	0.387	9.943	0.491	-6.155	9.848
111	5 <sup>h</sup> 25 <sup>m</sup> 05 <sup>s</sup> 343	69 <sup>d</sup> 38 <sup>m</sup> 08 <sup>s</sup> 948	-5.298	0.301	9.658	0.548	NA	NA
112	5 <sup>h</sup> 25 <sup>m</sup> 05 <sup>s</sup> 381	69 <sup>d</sup> 38 <sup>m</sup> 11 <sup>s</sup> 992	-6.841	0.346	10.297	0.521	NA	NA
113	5 <sup>h</sup> 25 <sup>m</sup> 05 <sup>s</sup> 438	69 <sup>d</sup> 38 <sup>m</sup> 10 <sup>s</sup> 191	-7.160	0.344	10.850	0.522	-6.155	9.848
114	5 <sup>h</sup> 25 <sup>m</sup> 04 <sup>s</sup> 640	69 <sup>d</sup> 38 <sup>m</sup> 10 <sup>s</sup> .040	-3.924	0.241	9.388	0.577	-7.386	9.848
115	5h25m04 s 454	69 <sup>d</sup> 38 <sup>m</sup> 09 <sup>s</sup> 844	-4.261	0.246	9.951	0.575	NA	NA
116	5 <sup>h</sup> 24 <sup>m</sup> 58 <sup>s</sup> 646	69 <sup>d</sup> 38 <sup>m</sup> 25 <sup>s</sup> .981	6.982	0.425	7.526	0.458	NA	NA
117	5h25m01 s 395	69 <sup>d</sup> 38 <sup>m</sup> 49 <sup>s</sup> 800	1.921	0.302	-3.487	0.547	NA	NA
118	5 <sup>h</sup> 25 <sup>m</sup> 01 <sup>s</sup> 442	69 <sup>d</sup> 38 <sup>m</sup> 50 <sup>s</sup> 223	0.035	0.005	-4.109	0.625	NA	NA
119	5 <sup>h</sup> 24 <sup>m</sup> 59 <sup>s</sup> .732	69 <sup>d</sup> 38 <sup>m</sup> 20 <sup>s</sup> 293	3.725	0.301	6.767	0.548	0.000	3.693
120	5 <sup>h</sup> 25 <sup>m</sup> 05 <sup>s</sup> 432	69 <sup>d</sup> 38 <sup>m</sup> 08 <sup>s</sup> 588	-6.583	0.334	10.405	0.528	NA	NA

**Note.** Positive values indicate the direction to the north and east in R.A. and decl., respectively. Results of the automated procedure are matched when applicable. (This table is available in machine-readable form.)

## **ORCID iDs**

John Banovetz https://orcid.org/0000-0003-0776-8859

Dan Milisavljevic https://orcid.org/0000-0002-0763-3885

Kathryn E. Weil https://orcid.org/0000-0002-8360-0831

Bhagya Subrayan https://orcid.org/0000-0001-8073-8731

Robert A. Fesen https://orcid.org/0000-0003-3829-2056

Daniel J. Patnaude https://orcid.org/0000-0002-7507-8115

Paul P. Plucinsky https://orcid.org/0000-0003-1415-5823

Charles J. Law https://orcid.org/0000-0003-1413-1776

William P. Blair https://orcid.org/0000-0003-2379-6518

Jon A. Morse https://orcid.org/0000-0001-5895-2256

### References

Ackermann, M., Albert, A., Atwood, W. B., et al. 2016, A&A, 586, A71 Astropy Collaboration, Price-Whelan, A. M., Sipőcz, B. M., et al. 2018, AJ, 156, 123

```
Bally, J., Reipurth, B., Walawender, J., & Armond, T. 2002, AJ, 124, 2152
Bamba, A., Ohira, Y., Yamazaki, R., et al. 2018, ApJ, 854, 71
Banas, K. R., Hughes, J. P., Bronfman, L., & Nyman, L. Å. 1997, ApJ,
  480, 607
Banovetz, J., Milisavljevic, D., Sravan, N., et al. 2021, ApJ, 912, 33
Bhalerao, J., Park, S., Schenck, A., Post, S., & Hughes, J. P. 2019, ApJ,
  872, 31
Blair, W. P., Morse, J. A., Raymond, J. C., et al. 2000, ApJ, 537, 667
Borkowski, K. J., Hendrick, S. P., & Reynolds, S. P. 2007, ApJL,
  671, L45
Borkowski, K. J., Miltich, W., & Reynolds, S. P. 2020, ApJL, 905, L19
Burrows, A., Radice, D., & Vartanyan, D. 2019, MNRAS, 485, 3153
Chen, Y., Zhang, F., Williams, R. M., & Wang, Q. D. 2003, ApJ, 595, 227
Chevalier, R. A. 2005, ApJ, 619, 839
Clark, D. H. 1982, Obs, 102, 111
Currie, D. G., Dowling, D. M., Shaya, E. J., et al. 1996, AJ, 112, 1115
Danziger, I. J., & Dennefeld, M. 1976, ApJ, 207, 394
Dickel, J. R., & Milne, D. K. 1995, AJ, 109, 200
Dopita, M. A., Vogt, F. P. A., Sutherland, R. S., et al. 2018, ApJS, 237, 10
```

Astropy Collaboration, Robitaille, T. P., Tollerud, E. J., et al. 2013, A&A,

```
Favata, F., Vink, J., Parmar, A. N., Kaastra, J. S., & Mineo, T. 1997, A&A,
  324, L45
Ferrand, G., Warren, D. C., Ono, M., et al. 2021, ApJ, 906, 93
Fesen, R. A. 2001, ApJS, 133, 161
Fesen, R. A., & Gunderson, K. S. 1996, ApJ, 470, 967
Fesen, R. A., Hammell, M. C., Morse, J., et al. 2006, ApJ, 645, 283
Fesen, R. A., & Milisavljevic, D. 2016, ApJ, 818, 17
Fesen, R. A., Zastrow, J. A., Hammell, M. C., Shull, J. M., & Silvia, D. W.
   2011, ApJ, 736, 109
Finkelstein, S. L., Morse, J. A., Green, J. C., et al. 2006, ApJ, 641, 919
Fox, O. D., Van Dyk, S. D., Williams, B. F., et al. 2022, ApJL, 929, L15
Gaensler, B. M., & Wallace, B. J. 2003, ApJ, 594, 326
Ghavamian, P., Hughes, J. P., & Williams, T. B. 2005, ApJ, 635, 365
Gonzaga, S., Hack, W., Fruchter, A., & Mack, J. 2012, The DrizzlePac
   Handbook
Graczyk, D., Pietrzyński, G., Thompson, I. B., et al. 2014, ApJ, 780, 59
Green, W. 2012, SASS, 31, 159
H. E. S. S. Collaboration, Abramowski, A., Aharonian, F., et al. 2015, Sci,
   347, 406
Hammell, M. C., & Fesen, R. A. 2008, ApJS, 179, 195
Hartigan, P., Morse, J. A., Reipurth, B., Heathcote, S., & Bally, J. 2001, ApJL,
   559, L157
Holland-Ashford, T., Lopez, L. A., Auchettl, K., Temim, T., &
  Ramirez-Ruiz, E. 2017, ApJ, 844, 84
Hughes, J. P. 1987, ApJ, 314, 103
Janka, H.-T., Melson, T., & Summa, A. 2016, ARNPS, 66, 341
Kamper, K., & van den Bergh, S. 1976, ApJS, 32, 351
Katsuda, S., Morii, M., & Janka, H.-T. 2018, ApJ, 856, 18
Kerzendorf, W. E., Do, T., de Mink, S. E., et al. 2019, A&A, 623, A34
Kiminki, M. M., Reiter, M., & Smith, N. 2016, MNRAS, 463, 845
Lang, D., Hogg, D. W., Mierle, K., Blanton, M., & Roweis, S. 2010, AJ,
   139, 1782
Lasker, B. M. 1980, ApJ, 237, 765
Law, C. J., Milisavljevic, D., Patnaude, D. J., et al. 2020, ApJ, 894, 73
Lee, J.-J., Park, S., Hughes, J. P., & Slane, P. O. 2014, ApJ, 789, 7
Li, C.-J., Seitenzahl, I. R., Ishioka, R., et al. 2021, ApJ, 915, 20
Long, X., Patnaude, D. J., Plucinsky, P. P., & Gaetz, T. J. 2022, ApJ, 932, 117
Lopez, L. A., & Fesen, R. A. 2018, SSRRv, 214, 44
Milisavljevic, D., & Fesen, R. A. 2013, ApJ, 772, 134
Milisavljevic, D., & Fesen, R. A. 2017, in Handbook of Supernovae, ed.
```

A. W. Alsabti & P. Murdin (Berlin: Springer), 2211

```
Milisavljevic, D., Fesen, R. A., Gerardy, C. L., Kirshner, R. P., & Challis, P.
  2010, ApJ, 709, 1343
Morse, J. A., Kellogg, J. R., Bally, J., et al. 2001, ApJL, 548, L207
Morse, J. A., Winkler, P. F., & Kirshner, R. P. 1995, AJ, 109, 2104
Murdin, P., & Clark, D. H. 1979, MNRAS, 189, 501
Orlando, S., Wongwathanarat, A., Janka, H. T., et al. 2021, A&A,
  645, A66
Orlando, S., Wongwathanarat, A., Janka, H. T., et al. 2022, A&A, 666, A2
Panagia, N., Gilmozzi, R., Macchetto, F., Adorf, H. M., & Kirshner, R. P.
  1991, ApJL, 380, L23
Park, S., Hughes, J. P., Slane, P. O., et al. 2007, ApJL, 670, L121
Patnaude, D. J., & Fesen, R. A. 2014, ApJ, 789, 138
Reed, J. E., Hester, J. J., Fabian, A. C., & Winkler, P. F. 1995, ApJ, 440, 706
Sano, H., Plucinsky, P. P., Bamba, A., et al. 2020, ApJ, 902, 53
Sasaki, M., Gaetz, T. J., Blair, W. P., et al. 2006, ApJ, 642, 260
Scowcroft, V., Freedman, W. L., Madore, B. F., et al. 2016, ApJ, 816, 49
Sharda, P., Gaetz, T. J., Kashyap, V. L., & Plucinsky, P. P. 2020, ApJ,
  894, 145
Silverman, B. W. 1982, Appl. Stat., 31, 67
Smartt, S. J. 2009, ARA&A, 47, 63
2000, Smithsonian Astrophysical ObservatorySAOImage DS9: A Utility for
  Displaying Astronomical Images in the X11 Window Environment,
  Astrophysics Source Code Library, ascl:0003.002
Sutherland, R. S., & Dopita, M. A. 1995, ApJ, 439, 365
Temim, T., Slane, P., Raymond, J. C., et al. 2022, ApJ, 932, 26
Thorstensen, J. R., Fesen, R. A., & van den Bergh, S. 2001, AJ, 122, 297
Vink, J., Patnaud, D. J., & Castro, D. 2022, ApJ, 929, 57
Vogt, F., & Dopita, M. A. 2011, AP&SS, 331, 521
Vogt, F. P. A., Bartlett, E. S., Seitenzahl, I. R., et al. 2018, NatAs, 2, 465
Vogt, F. P. A., Seitenzahl, I. R., Dopita, M. A., & Ghavamian, P. 2017, A&A,
Weil, K. E., Fesen, R. A., Patnaude, D. J., et al. 2020, ApJ, 891, 116
Westerlund, B. E., & Mathewson, D. S. 1966, MNRAS, 131, 371
Williams, B. J., Borkowski, K. J., Reynolds, S. P., et al. 2006, ApJL,
  652, L33
Winkler, P. F., Garber, J. H., Plunkett, A. L. D., Twelker, K., & Long, K. S.
  2010, AAS HEAD Meeting, 11, 18.13
Winkler, P. F., Twelker, K., Reith, C. N., et al. 2009, ApJ, 692, 1489
Wongwathanarat, A., Müller, E., & Janka, H. T. 2015, A&A, 577, A48
Xi, L., Gaetz, T. J., Plucinsky, P. P., Hughes, J. P., & Patnaude, D. J. 2019,
   ApJ, 874, 14
```